

Direct numerical simulation of stenotic flows, Part 2: Pulsatile flow

By **SONU S. VARGHESE¹**, **STEVEN H. FRANKEL¹**
AND **PAUL F. FISCHER²**

¹School of Mechanical Engineering, Purdue University, 585 Purdue Mall, West Lafayette, IN 47907, USA

²Mathematics and Computer Science Division, Argonne National Laboratory, Argonne, IL 60439, USA

(Received 28 January 2005)

Direct numerical simulations (DNS) of stenotic flows under conditions of steady inlet flow were discussed in Part 1 of this study. DNS of pulsatile flow through the 75% stenosed tube (by area) employed for the computations in Part 1 is examined here. Analogous to the steady flow results, DNS predicts a laminar post-stenotic flowfield in the case of pulsatile flow through the axisymmetric stenosis model, in contrast to previous experiments, in which intermittent disturbed flow regions and turbulent breakdown were observed in the downstream region. The introduction of a stenosis eccentricity, that was 5% of the main vessel diameter at the throat, resulted in periodic, localized transition to turbulence. Analysis in this study indicated that the early and mid-acceleration phases of the time period cycle were relatively stable, with no turbulent activity in the post-stenotic region. However, towards the end of acceleration, the starting vortex, formed earlier as the fluid accelerated through the stenosis at the beginning of acceleration, started to break up into elongated streamwise structures. These streamwise vortices broke down at peak flow, forming a turbulent spot in the post-stenotic region. The early part of deceleration witnessed intense turbulent activity within this spot. Past the mid-deceleration phase, through to minimum flow, the inlet flow lost its momentum and the flowfield began to relaminarize. The start of acceleration in the following cycle saw a recurrence of the entire process of a starting structure undergoing turbulent breakdown and subsequent relaminarization of the post-stenotic flowfield. Peak wall shear stress (WSS) magnitudes occurred at the stenosis throat and close to the reattachment location during most of the acceleration phase, with the rest of the vessel experiencing much lower levels of WSS. Turbulent breakdown at peak flow resulted in a sharp amplification of WSS levels across the region corresponding to the turbulent spot, accompanied by large axial and circumferential fluctuations. Magnitudes dropped rapidly after the mid-deceleration phase, when the relaminarization process took over.

1. Introduction

Part 1 (Varghese, Frankel & Fischer 2005) of this study dealt with steady flow through both axisymmetric and eccentric stenosis models, with the geometry and flow conditions selected to match the classic stenotic flow experiments of Ahmed & Giddens (1983a). For the range of Reynolds numbers considered, the numerical simulations under steady inlet conditions predicted laminar flow in the case of the axisymmetric model, with no disturbances whatsoever, downstream of the stenosis throat (neck). In contrast, the in-

roduction of a small eccentricity within the stenosis, 5% of the main vessel diameter at the throat, resulted in localized transition to turbulence in the region beyond six vessel diameters downstream of the throat for the highest Reynolds number considered. The nature of the turbulence was found to closely resemble localized structures observed during pipe flow transition at similar Reynolds numbers. As a result of turbulent breakdown, large spatial variations of wall shear stress were observed along the post-stenotic walls.

The steady flow results provide an insight into the complexities that may arise in the presence of a stenosis and serve as a precursor to more physiologically realistic pulsatile flow simulations. The complex flow features seen in the steady flow case, involving flow separation, recirculation, reattachment, and strong shear layers, when combined with flow pulsatility, can result in periodic transition to turbulence downstream of the stenosis. This paper discusses pulsatile flow results obtained by using the same stenoses models used for the steady flow simulations under flow conditions matching those of Ahmed & Giddens (1984), with the intention of complementing earlier stenotic flow studies and providing a fundamental basis for understanding the flow dynamics that influence variables such as wall shear stress, which have been found to play a role in the progression of arterial disease (Ku 1997).

The spectral-element code employed here was designed specifically for simulating transitional flows in complex geometries (Fischer, Kruse & Loth 2002); details on the numerical methodology are given in Part 1. The flow model and data reduction procedure are outlined in §2. As in Part 1, comparisons with experiments are included in the results and discussion presented in §3. Conclusions follow at the end.

2. Problem formulation

2.1. Flow model and dimensionless groups

The axisymmetric and eccentric stenosis geometries modeled in this study were similar to those introduced in Part 1, matching the models employed in the stenotic flow experiments of Ahmed & Giddens (1983a, 1984). The stenosis axis was offset by $0.05D$, D being the vessel diameter, in the eccentric model. For the pulsatile flow simulations reported in this paper, the Womersley solution (Womersley 1955) for laminar, pulsatile flow through rigid tubes was used as the inlet boundary condition. It was specified as

$$\frac{u}{u_c} = [1 - r^2] + A \left[\frac{1 - J_0(i^{3/2}\alpha \frac{2r}{D})}{J_0(i^{3/2}\alpha)} \right] \sin(\omega t), \quad (2.1)$$

where u_c is the mean (cycle-averaged) centerline inlet velocity, A is the amplitude of pulsation, $J_0()$ is the Bessel function of type 0, ω is the angular frequency of pulsation, and α is the non-dimensional Womersley parameter ($= \frac{D}{2}\sqrt{\omega\nu}$, with ν being the kinematic viscosity). While the Reynolds number provides a measure of the ratio between inertial and viscous forces, the Womersley number offers a measure of the relative strength of unsteady and viscous forces, with unsteady inertial forces dominating for $\alpha > 10$ (Ku 1997).

In both the axisymmetric and eccentric models, the upstream and downstream sections of the vessel extended for three and sixteen vessel diameters, respectively, as measured from the stenosis throat. Rigid vessel walls were assumed throughout, with the no-slip condition applied at the vessel walls. The outflow boundary condition treatment discussed in Part 1 of this study (Varghese *et al.* 2005) was employed for the current simulations as well, effectively adding a constant to the outward normal component of the velocity field to ensure that the characteristics are always pointing outwards, as if forcing the

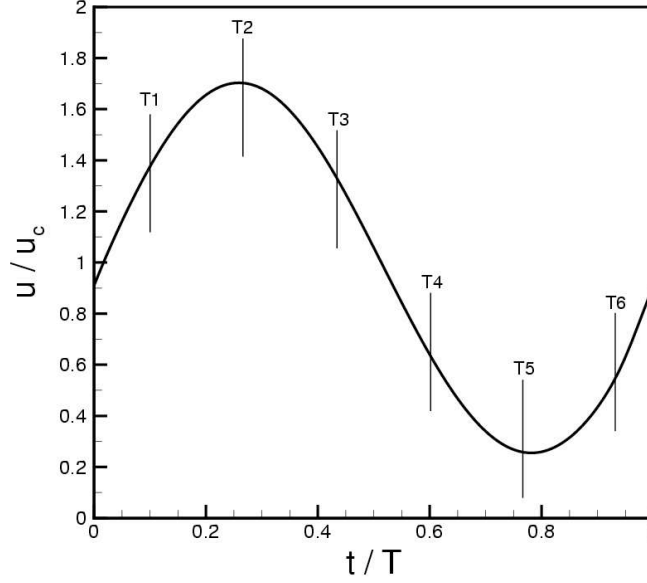


FIGURE 1. Axial centerline velocity at the vessel inlet. Reference times at which results were obtained are also indicated.

flow through a nozzle. The effect of this treatment was confirmed to be restricted to the outflow region, $x > 15.5D$, for all the cases reported here.

All parameters and normalizations employed in this study were chosen to replicate the flow conditions in the experiments by Ahmed & Giddens (1984) to facilitate comparison with their measurements. The Reynolds number based on the main vessel diameter, D , and mean inlet centerline velocity, u_c , was 600, with minimum and maximum Reynolds of approximately 200 and 1000, respectively, corresponding to a value of $A = 0.667$ in equation (2.1). The Womersley number, α , was chosen as 7.5. The velocity waveform at the inlet was sinusoidal, as the boundary condition in equation (2.1) defines, and the resulting inlet centerline velocity is shown in figure 1. Results presented in the following sections were obtained at intervals of $T/6$ (T being the period of pulsation). The six phases in the pulsatile cycle, indicated in figure 1, were deemed sufficient to accurately represent the temporal evolution of the flow.

2.2. Data reduction

In unsteady flows, similar to the pulsatile flow cases studied here, several types of averaging operations can be employed. For a generic flow variable f , the time-averaged mean over a period of time T_f is computed as

$$\bar{f}(x, y, z) = \frac{1}{T_f} \int_{t_0}^{t_0+T_f} f(x, y, z, t) dt, \quad (2.2)$$

where t_0 is the time at which the averaging process is initiated. The deviation from this average, which represents random turbulent fluctuations, is then defined as

$$f'(x, y, z, t) = f(x, y, z, t) - \bar{f}(x, y, z). \quad (2.3)$$

The time-averaging operation defined in equation (2.2) is typically employed to analyze steady flow data, as in Part 1. In case of pulsatile flow, $T_f = NT$, where N is the number

of time period cycles over which time integration is performed and T is the time period of each pulsatile cycle. Additionally, a phase-averaging operator that represents the time-varying coherent response to the pulsatility (Lieber & Giddens 1988; Scotti & Piomelli 2001a; Mittal, Simmons & Najjar 2003) can be defined over N time period cycles as

$$\langle f \rangle(x, y, z, t) = \frac{1}{N} \sum_{n=0}^{N-1} f(x, y, z, t + nT). \quad (2.4)$$

In order to distinguish between the scales associated with pulsation and those from random turbulent motions, the fluctuation with respect to the phase average, differentiated from the time average fluctuation in equation (2.3) by using a double prime, is defined as

$$f''(x, y, z, t) = f(x, y, z, t) - \langle f \rangle(x, y, z, t). \quad (2.5)$$

The root mean square (*r.m.s.*) quantities are computed as

$$f''_{r.m.s.} = \sqrt{\langle f''^2 \rangle}. \quad (2.6)$$

2.3. Simulation details

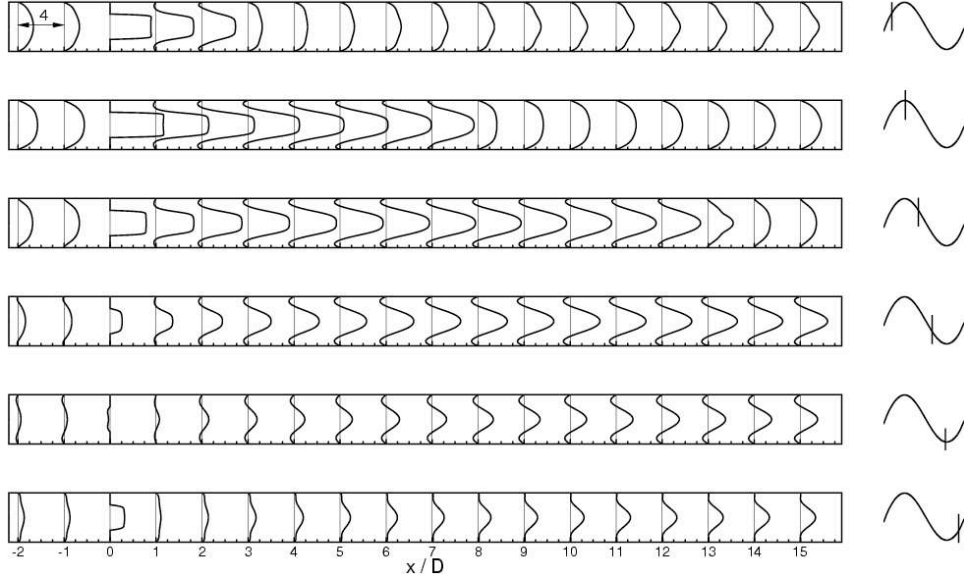
Simulation of pulsatile flow through the axisymmetric stenosis was conducted with a polynomial order of $N = 9$ on a mesh comprising $K = 1600$ hexahedral cells (N and K are defined in Part 1 of this study) and the mesh was found to be adequate for this case. The corresponding eccentric model simulations were conducted with $N = 12$ on a mesh with $K = 2400$ cells to obtain sufficient resolution. Increasing the polynomial order to $N = 14$ for the latter case did not change the solution by more than 3% and so results obtained on the $K = 2400$, $N = 12$ mesh are presented in the following sections.

The axisymmetric model computation was initiated from steady flow results obtained at $Re = 500$, presented in Part 1, while the eccentric case employed results from the axisymmetric case as the initial condition. In both cases, initial transients were ensured to have left the computational domain and results presented in the following sections are independent of the initial conditions. A non-dimensional time step size of $1.0e-3$ was used for simulating pulsatile flow through the axisymmetric stenosed vessel but this had to be lowered to $2.5e-4$ for the eccentric model, in which flow transitioned to turbulence, and consequently, the most computationally challenging simulation. Simulation of one time periodic cycle through the axisymmetric model required less than a day on 32 processors of an AMD Athlon based Linux cluster, while the corresponding time for the eccentric case was six days.

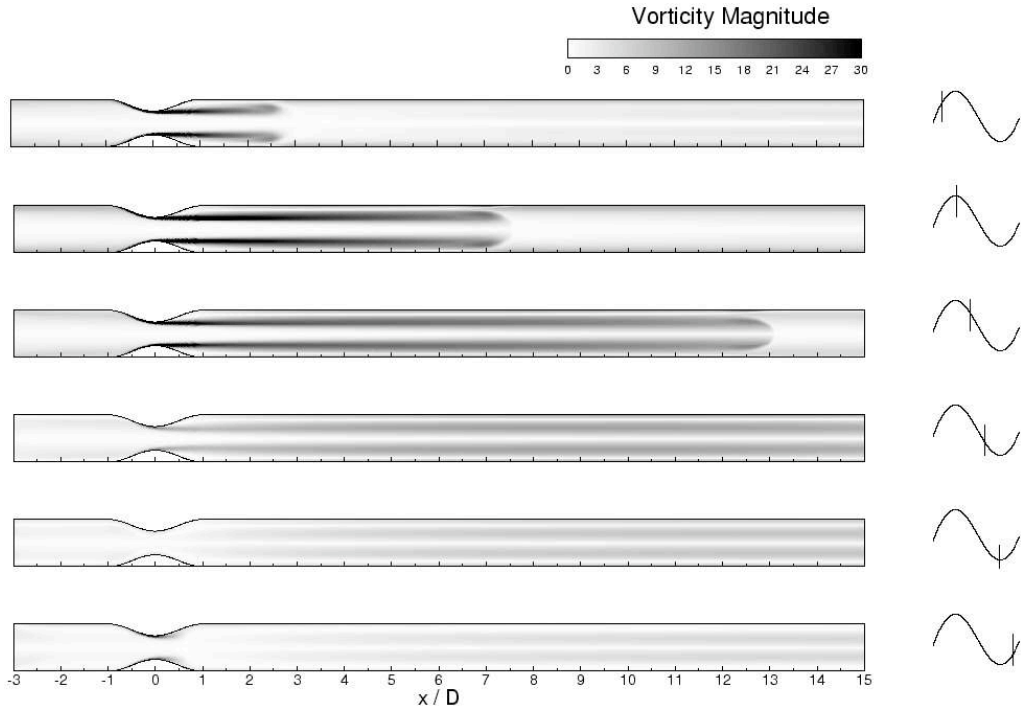
3. Results and discussion

3.1. Axisymmetric model

Figure 2 (a) and (b) show axial velocity profiles and vorticity magnitude contours, respectively, from the simulation of pulsatile flow through the axisymmetric stenosis. The velocity profiles upstream of the stenosis closely correspond to the Womersley solution as defined in equation (2.1). Past the mid-acceleration phase, the flow upstream almost resembles the parabolic profile seen in fully developed steady pipe flow. The upstream centerline velocity is about 1.4 times the mean inlet centerline velocity (u_c) at this point. As in the steady flow case, the flow rapidly accelerates through the stenosis creating a plug-shaped profile at the throat with peak velocities greater than $3.65u_c$. The stenotic jet and separation region that forms immediately downstream of the stenosis extend past



(a)



(b)

FIGURE 2. Pulsatile flow through the 75% axisymmetric stenosis at mean inlet $Re = 600$. (a) Sequence of axial velocity profiles, normalized by mean inlet centerline velocity u_c , and (b) sequence of vorticity magnitude contours, normalized by u_c/D .

the $x = 2D$ axial station at this time, even as the flowfield in the region beyond $x = 3D$ is still recovering from the activity of the stenotic jet that traversed the post-stenotic section during the previous cycle. The corresponding sequence of vorticity magnitude contours in figure 2(b) shows the vortex ring at the front of the jet propagating downstream over the course of the cycle, followed by a trail of vorticity that extends back to the stenosis throat, where the shear layer was first created. At this phase, the vortex ring is located between $x = 2D$ and $3D$.

The vortex ring moves past the $x = 7D$ station at the phase when maximum flow conditions exist at the inlet, indicating that the vortex traveled about five vessel diameters within a time span of $T/6$. As the inlet flow reaches peak acceleration, peak velocities at the throat rise to approximately $4.65u_c$, and the centerline velocity at the jet front is greater than $3.6u_c$. In spite of subsequent flow deceleration at the inlet, the results show that the jet continues to propagate downstream at an almost constant speed over the $T/6$ interval following peak flow, with the vortex ring and separation zone moving past the $x = 12D$ axial station during early deceleration. At this phase, the peak jet velocity drops to about $3.1u_c$ and $3.5u_c$ at the throat and jet front, respectively. As deceleration continues past the halfway point, the trailing shear layer at the stenosis throat dies away, and the vortex ring convects out of the domain before the inlet flow reaches a minimum. Flow separation extends over the entire post-stenotic section during this late stage of deceleration. At the same time, the adverse pressure gradient during this phase results in the dominance of viscous effects over inertial forces in the near-wall region, and a small separation region forms upstream of the stenosis, as evidenced by the profiles at $x = -1D$ and $-2D$.

Flow separation in the upstream section continues through the cycle until minimum inlet flow conditions, with upstream centerline velocities dropping to less than $0.3u_c$ by this time. The adverse pressure gradient at this point in the cycle is large enough to create a small flow reversal region at the stenosis throat, as a result of which the shear layer completely detaches itself from the stenosis. As the pressure gradient once again becomes favorable in the early part of the acceleration phase, the flow starts to accelerate again, and the beginnings of a new jet can be seen forming during early acceleration. A new shear layer starts to form at the lip of the stenosis, even as the shear layer created during the previous cycle continues to lose its strength and is eventually pushed out of the domain. The velocity profiles also indicate that the flow has completely reattached to the wall, both upstream and downstream of the stenosis, by this time. There is no permanent recirculation region in the downstream flowfield, in contrast to the post-stenotic flowfield observed under steady inlet conditions.

Computed axial velocity profiles during peak inlet flow conditions are compared with experimental measurements by Ahmed & Giddens (1984) in figure 3. As in the steady flow axisymmetric model, profiles computed downstream of a 73% stenotic occlusion are also included in the comparisons. The results predicted for the 73% model are in much better agreement with the experiments at all locations considered, similar to the comparisons made for the steady flow case in Part 1 of this report. Only at $x = 4D$ and $6D$ is there a small disagreement between the profiles, especially in the near-wall region, with flow appearing to reattach a little earlier in the experiments. These differences, which are less than 5%, are smaller than those observed under steady flow conditions, where differences were between 15 and 20% in the vicinity of the experimental reattachment location. Experimental measurements downstream of $x = 6D$ were not available.

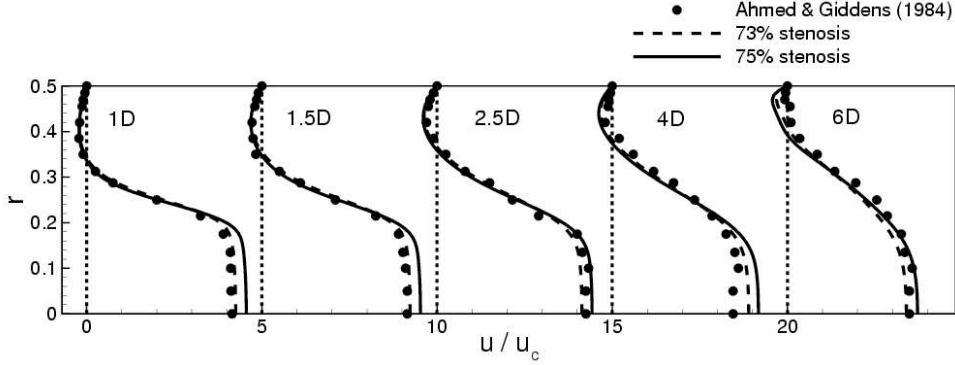


FIGURE 3. Comparison of axial velocity profiles at downstream locations with experimental profiles for pulsatile flow through the axisymmetric stenosis, under conditions of peak flow at the inlet. The axial stations are indicated in terms of diameters downstream from the stenosis throat.

3.2. Eccentric model - Transition to turbulence

Under similar flow conditions (same Reynolds and Womersley numbers) to those used for the axisymmetric model described in the previous section, the introduction of a geometric perturbation, in the form of a $0.05D$ eccentricity at the stenosis throat, causes the flow to deviate markedly from axisymmetry. The pulsatility contributes to periodic localized transition to turbulence during the deceleration phase and subsequent relaminarization during the acceleration part of the cycle, as will be detailed in this section. The phase-averaging operation defined in equation (2.4) was employed to present results for this case, where the statistics were gathered over a total of 10 (N in that equation) flow cycles. The simulation was run for three flow cycles before the statistics were gathered, to minimize the influence of any initial transients on the statistical results.

3.2.1. Evolution of averaged flow characteristics

Figures 4 and 5 shows phase-averaged axial velocity profiles and vorticity magnitude contours, respectively, in both the vessel bisecting planes. The results obtained along the two planes considered illustrate the spatial evolution of the flow throughout the pulsatile cycle and the breaking of axisymmetry in the downstream flowfield as a result of the eccentricity. During the later stages of acceleration, the velocity and vorticity plots in the plane of eccentricity ($y = 0.0$) show the plug-shaped jet, formed as the flow accelerates through the constriction, being deflected toward the side of the eccentricity. The velocity profiles in both planes of interest reveal the extent of the resulting asymmetric recirculation zone that forms immediately downstream of the stenosis. In keeping with the spatial evolution of flow observed for the axisymmetric case, the jet and accompanying flow separation zones along the walls extend only past the $x = 2D$ station at this stage, beyond which the flow continues to recover from the activity of the previous cycle. In fact, the profiles indicate that the flow in the far downstream section has not yet regained its upstream character by this late stage of acceleration, even though it achieves axisymmetry after $x \approx 9D$. Some evidence of shear layer roll-up at the forefront of the jet can be seen in the vorticity results along the $y = 0.0$ plane. This is reminiscent of the Kelvin-Helmholtz instability typically seen in free shear flows and indicates that the shear layer becomes increasingly unstable toward the end of acceleration, a manifestation of the highly inflectional velocity profiles in this region.

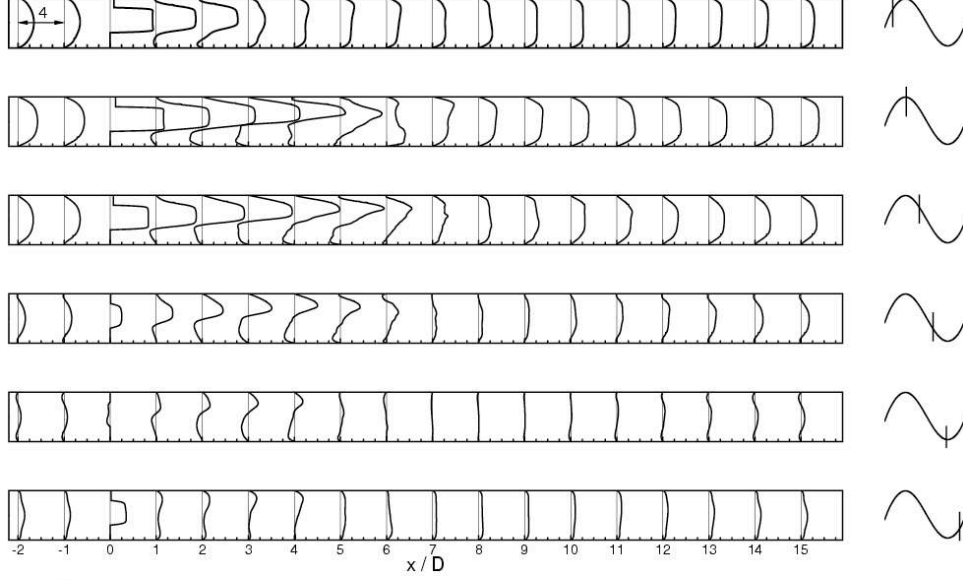
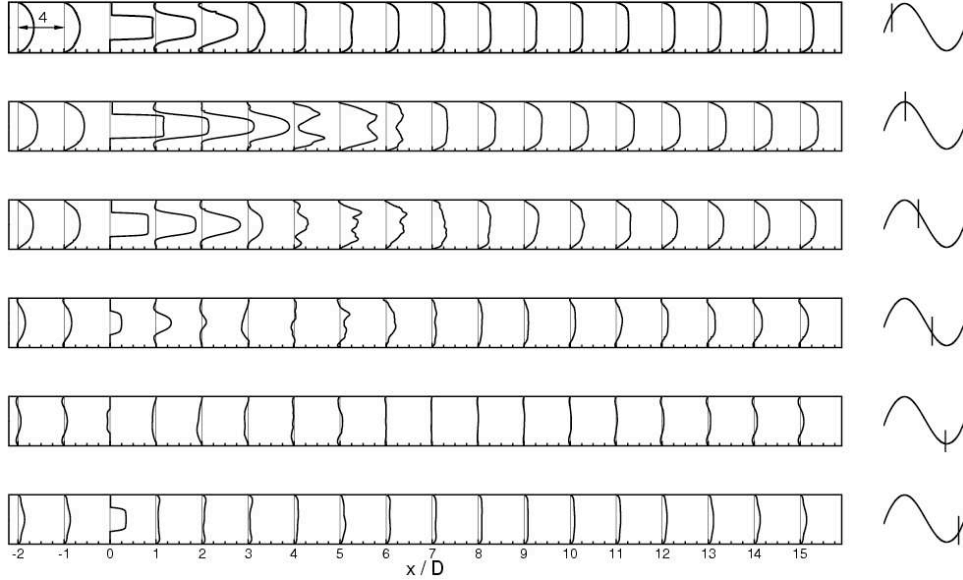
x - z plane, $y = 0.0$ x - y plane, $z = 0.0$ 

FIGURE 4. Sequence of phase-averaged axial velocity profiles, normalized by mean inlet centerline velocity u_c , for pulsatile flow through the 75% eccentric stenosis.

The vorticity magnitude contours in figure 5 shows that with the reversal of the pressure gradient at peak inlet flow, the jet and shear layer break down as they are deflected away from the wall at $x \approx 4D$; the flow apparently undergoing transition to turbulence subsequently, between $x = 4D$ and $6D$. The increased mixing in this region as a result of the unstable jet unsuccessfully attempting to negotiate the wall boundary constraint leads to complete flow reattachment by $x = 6D$. The velocity profiles in the turbulent

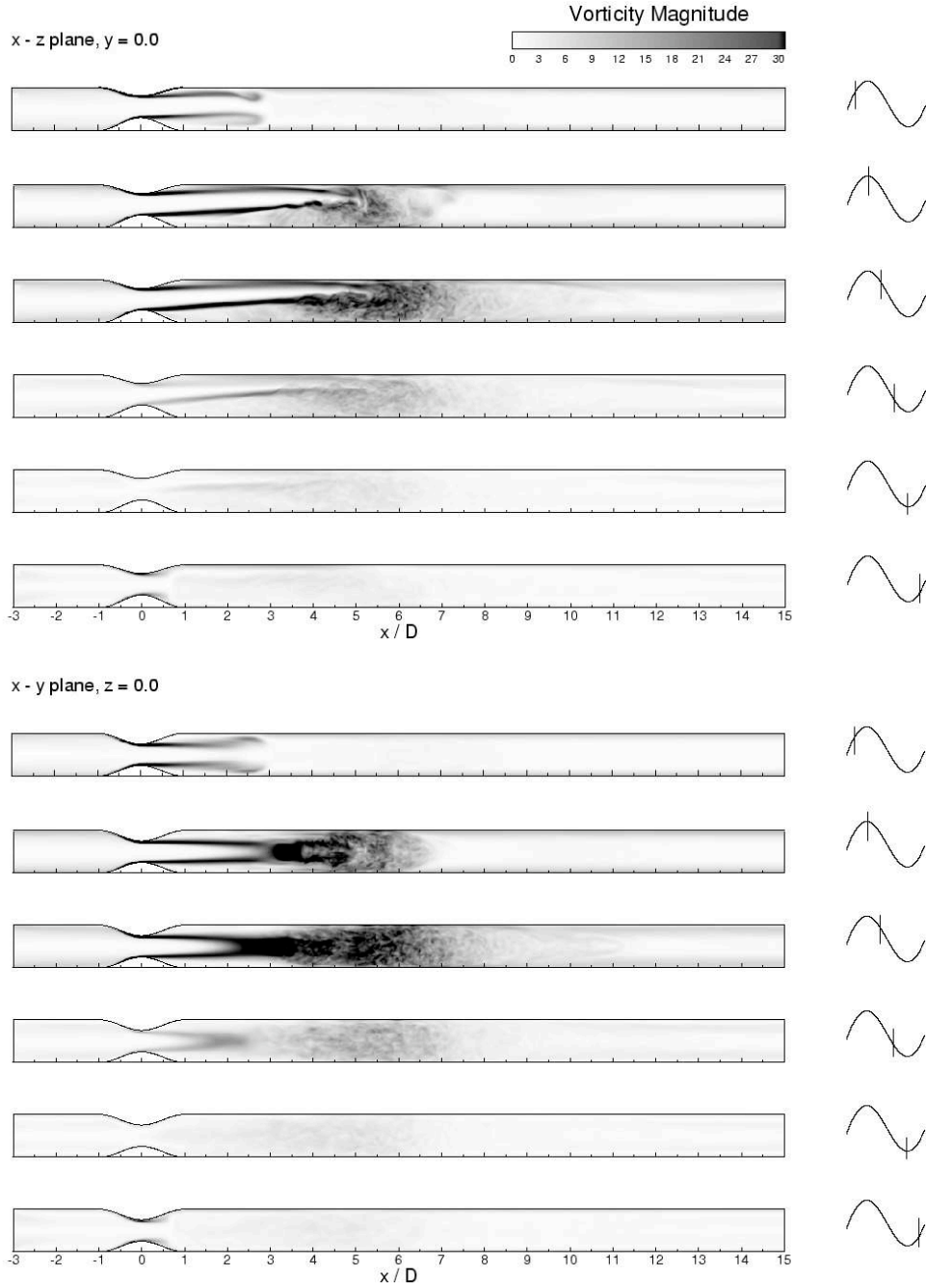


FIGURE 5. Sequence of phase-averaged vorticity magnitude contours, normalized by u_c/D , for pulsatile flow through the 75% eccentric stenosis.

region, $x = 5D$ to $7D$, start to lose their jet-like character and tend toward uniformity, unlike the continuing jet-like characteristics of corresponding velocity profiles obtained during peak flow conditions for the axisymmetric case, shown in figure 2(a).

The turbulent breakdown of the jet continues into the first half of the deceleration

phase, dominating the post-stenotic region between $x = 4D$ and $7D$. In the axisymmetric model, flow separation extended as far as $x = 12D$ at the beginning of deceleration, whereas in the eccentric model, separation is present only till $x \approx 6D$, beyond which the velocity profiles resemble the uniform profiles common to turbulent flows. The flowfield in the far downstream region is laminar, with the profiles in both planes regaining their upstream character after $x \approx 11D$.

The flow separation regions that were formed immediately downstream of the stenosis toward the end of the acceleration phase are present throughout the deceleration part of the cycle. However, the reattachment point stays stationary, lying between $x = 7D$ and $8D$, unlike the axisymmetric case in which the reattachment point moved farther downstream as deceleration progressed. Past the mid-deceleration point, viscous effects start to dominate the flowfield, and the shear layer begins to weaken. The profiles indicate that the flowrate reduces considerably during the late stages of deceleration and the recirculation regions start to recede, even as the small upstream separation region seen in the axisymmetric model forms close to the walls. The shear layer eventually detaches itself from the stenosis lip under minimum inlet flow conditions.

The velocity profiles in the region beyond $x > 7D$ during the late stages of deceleration and even minimum flow illustrate that the turbulent activity that occurred earlier in the cycle completely destroys any effect of the stenosis on the flowfield in the far downstream region, in sharp contrast to the jet-like character of the profiles predicted for the axisymmetric case close to the outflow boundary. For the eccentric case, throughout the deceleration phase, figure 4 shows that for $x > 11D$ the profiles in both planes closely resemble their upstream counterparts, indicating that the flow has completely relaminarized and regained its axisymmetry this far downstream of the stenosis. This situation occurs even in the early acceleration phase, which once again sees the formation of a new jet and shear layer as the flowrate increases. Forward flow exists across the entire vessel during these initial stages of the cycle when a favorable pressure gradient exists, with post-stenotic separation zones created only as the flowrate passes the halfway point of acceleration.

3.2.2. *Unsteady recirculation regions*

A closer look at the behavior of the recirculation regions is worthwhile because these directly correspond to locations of low wall shear stress along the post-stenotic vessel walls, a factor that has been implicated in atherosclerotic disease progression. The effect of the eccentricity in this regard is critical in that the size of the recirculation regions downstream of the stenosis is significantly larger than the size of those observed in the post-stenotic region of the axisymmetric stenosis model. Figure 6 shows phase-averaged, in-plane velocity vectors superimposed on axial velocity contours. Reverse flow regions have been highlighted by blanking out positive axial flow regions.

With the flow picking up momentum past the halfway point of acceleration, asymmetric flow separation forms immediately downstream of the stenosis as the fluid accelerates through the throat. Recirculation regions form along the side of the vessel opposite the side that is in closer proximity to the stenosis, as a result of the eccentricity, and toward which the jet is initially deflected. At this stage, the forefront of the stenotic jet at $x \approx 3D$ appears relatively undisturbed, with cross-stream velocities directing fluid toward the low-pressure region created by the jet at the vessel core. The downstream recirculation zones grow rapidly toward the end of acceleration; at peak flow, intense reverse flow regions form between $x = 2D$ and $3D$, even as cross-stream velocities larger than $0.5u_c$ after the latter axial station serve to reduce the size of these regions by entraining more fluid into the same. As a result of jet breakdown and increased mixing in the region

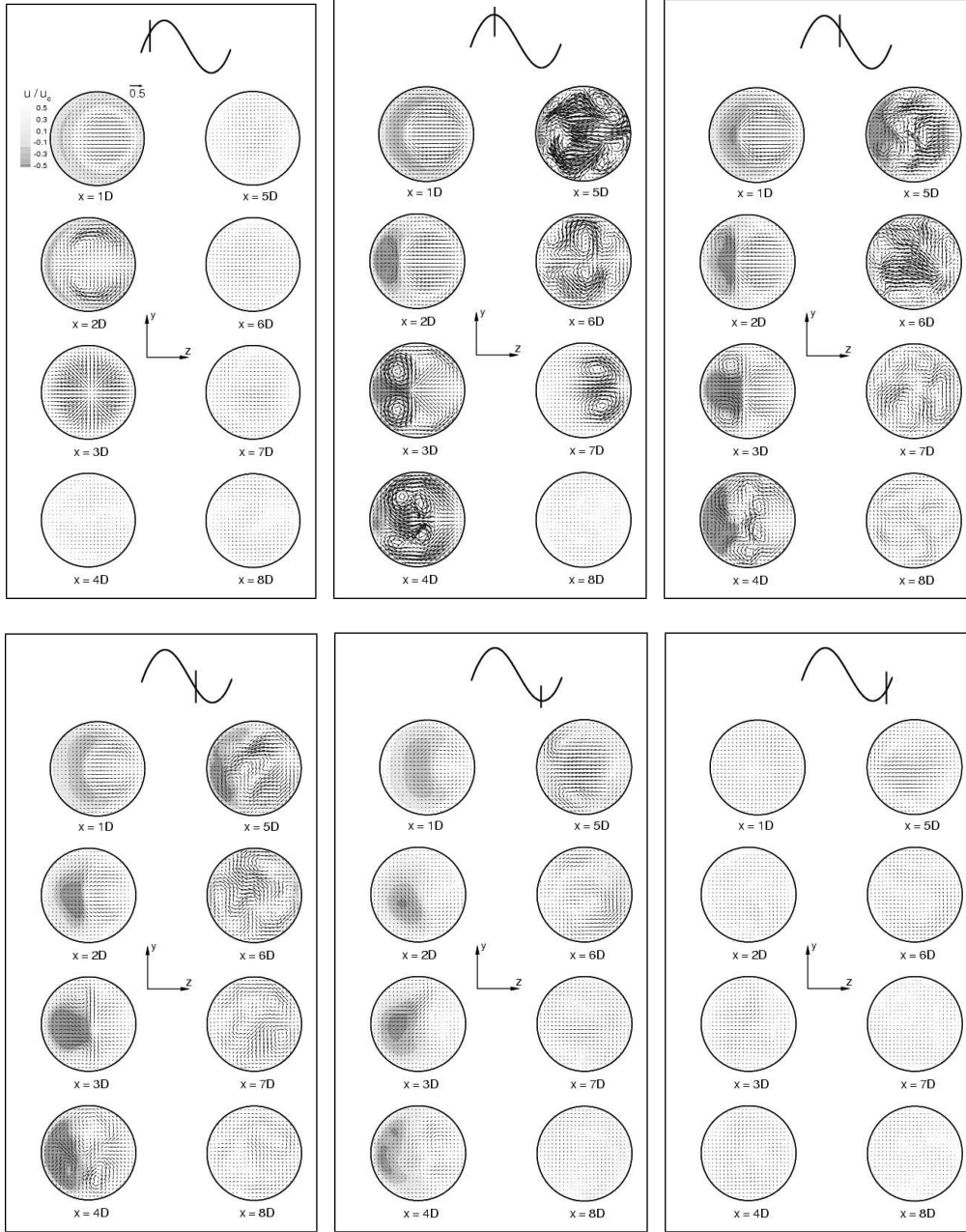


FIGURE 6. Phase-averaged results for pulsatile flow through the 75% eccentric stenosis showing in-plane velocity vectors superimposed on axial velocity contours at downstream stations. Axial velocity levels above 0.0 have been blanked out to highlight reverse flow regions. All three components of velocity have been normalized by u_c .

$x > 3D$, as the large in-plane velocity vectors ($> 0.5u_c$ at $x = 4D$ and $5D$) indicate, complete flow reattachment occurs by $x \approx 6D$, almost two vessel diameters earlier than in the axisymmetric model. The phase-averaged profiles in figure 4 indicate that the mean reverse flow between $x = 2D$ and $4D$ is about $0.5u_c$, which, again is in contrast to the

axisymmetric case, where the mean reverse flow was less than $0.25u_c$ during peak inlet flow and remained so throughout the remainder of the cycle. Also, the point of maximum reverse flow (as observed from the profiles in the $y = 0.0$ plane), which is 100% of u_c at $x = 3D$, moves closer to the walls with increasing axial distance from the throat, while at the same time dropping in magnitude.

The core of the recirculation zones moves farther downstream and continues moving closer to the walls throughout the deceleration phase, even as these regions attain their maximum cross-sectional extent around $x = 4D$ during this stage of the cycle. Maximum reverse flow levels, greater than 100% of u_c , occur between $x = 3D$ and $5D$. The mean reverse flow in these regions is more than 50% of u_c through most of deceleration, but rapidly drops to less than 20% by the point of minimum inlet flow. In the early stages of deceleration, cross-stream velocities are of the order of $0.5u_c$ in the breakdown region between $x = 4D$ and $6D$, and the point of complete flow reattachment shifts further downstream by about one vessel diameter, from $x \approx 6D$ at peak flow to $x \approx 7D$. Figure 6 shows a significant reduction in size of the recirculation zones toward the end of deceleration such that they occupy only a small area of the vessel cross-section at minimum flow. They disappear completely during the early stages of acceleration, confirming that a permanent recirculation zone is absent, as in the axisymmetric model.

We note that mean flow characteristics such as the results in figure 4 and figure 6 serve only to provide a highlight of post-stenotic reverse flow activity and may not reveal the precise unsteady nature of the flow in the recirculation regions; instantaneous snapshots are required to obtain a clearer picture.

3.2.3. *Temporal evolution*

Figure 7(a) shows the time history of instantaneous axial velocity at several axial stations along the centerline of the vessel, featuring flow disturbances as they appear downstream of the stenosis with each new cycle. The corresponding cycle or phase-averaged velocity waveforms in figure 7(b) highlight the temporal evolution (through one cycle) of the disturbances that are actually periodic and coherent. The jet-like effect created by the stenosis is apparent, as peak centerline velocity increases from about $1.7u_c$ at $x = 1D$ to $4.5u_c$ at the throat ($x/D = 0$) and eventually reduces to about $1.5u_c$ at $x = 8D$. These results match exactly the measurements made by Khalifa & Giddens (1981) in their study of post-stenotic disturbances for a 75% axisymmetric stenosis.

While the centerline velocity at the throat ($x/D = 0$) maintains the precise sinusoidal nature of the inlet velocity waveform, albeit with higher peak levels because of the flow accelerating through the constriction, the waveform loses this characteristic farther downstream. The formation of the starting vortex immediately downstream of the stenosis at the beginning of the acceleration phase is manifested in the flattening of the velocity waveform at $x = 1D$, after the point of minimum flow in the cycle, $t/T \approx 0.8$. The disturbance associated with this spatially and temporally evolving start-up structure becomes more pronounced as it moves further down the vessel. At $x = 3D$ the time history plots show a well-defined disturbance associated with the passage of a fairly evolved structure during the late acceleration stage, followed by random fluctuations throughout the deceleration phase. The phase-averaged results confirm the periodicity of these disturbances even though the deceleration disturbances may not be readily apparent on the scale used for these plots.

The subsequent breakup of the structures as they convect downstream is characterized by the high-frequency fluctuations that occur around peak flow at axial stations between $x = 4D$ and $7D$. Figure 7(a) indicates that the fluctuations grow to be particularly intense in this turbulent section of the post-stenotic vessel during the early part of deceleration

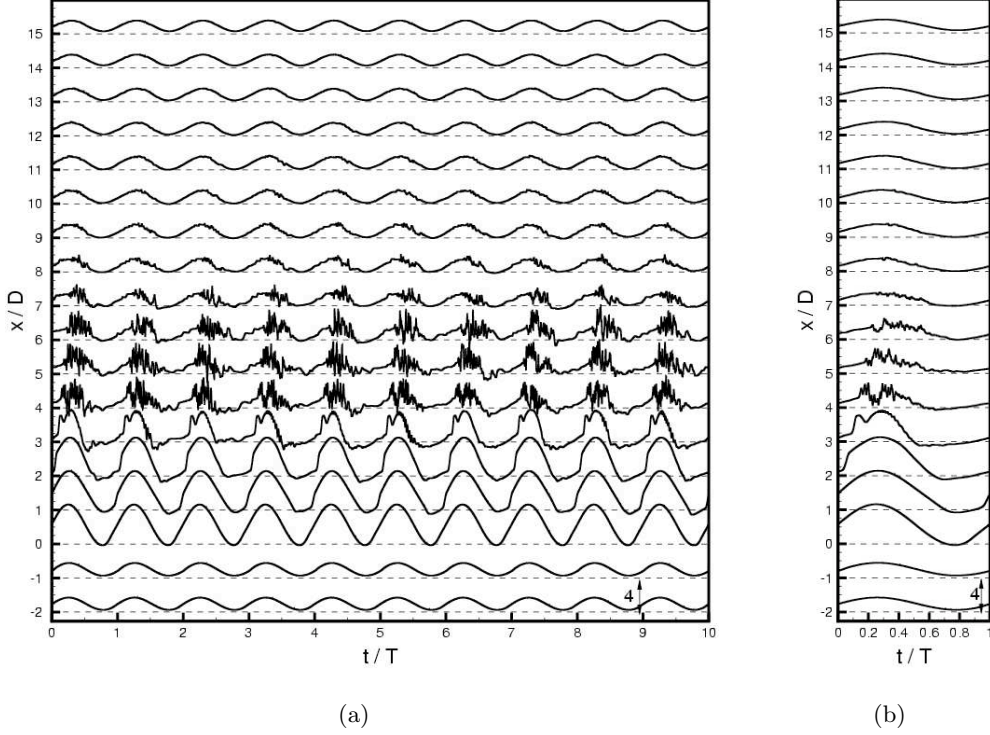


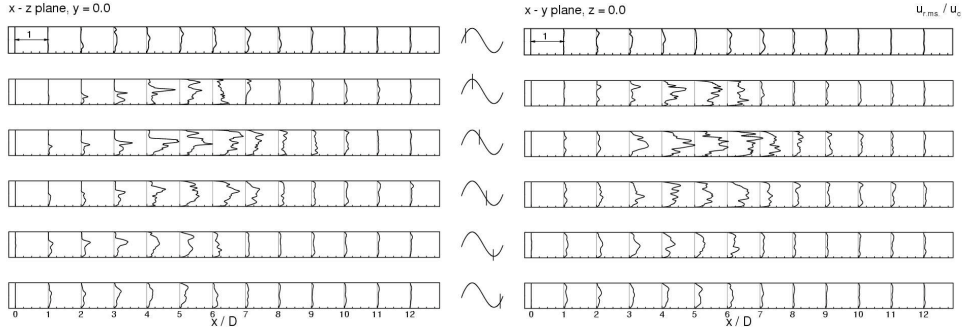
FIGURE 7. (a) Time history (over 10 cycles) of normalized centerline axial velocity, u/u_c , as a function of axial distance for pulsatile flow through the 75% eccentric stenosis. (b) Normalized phase-averaged centerline axial velocity, $\langle u \rangle / u_c$, as a function of axial distance.

and that they are repeated from cycle to cycle. The fluctuations reduce in intensity as minimum flow is approached. The presence of a similar pattern of disturbances between $x = 4D$ and $7D$ in the phase-averaged velocity results of figure 7(b) indicates that this phenomenon of localized transition to turbulence during peak flow and deceleration, followed by relaminarization, is indeed periodic. Beyond $x = 8D$, the intense fluctuations decay quite rapidly within about four vessel diameters, with the velocity waveforms after $x = 12D$ reverting to their laminar, upstream character. The flowfield appears to be stable at all axial locations considered here during the early and mid-acceleration phases of the cycle.

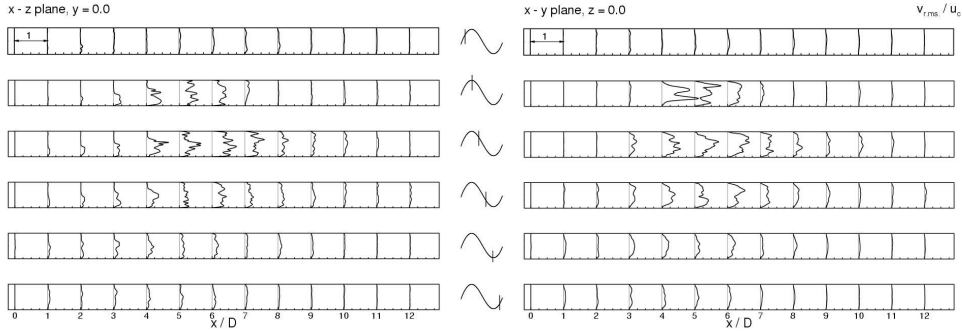
3.2.4. Turbulence statistics

Profiles of the streamwise and cross-stream *r.m.s.* velocities, as defined in § 2.2, are shown in figure 8, providing a quantifiable measure of turbulence intensity at different times during the cycle across the entire vessel. The corresponding spatial evolution of the turbulent kinetic energy, with k defined as $\frac{1}{2} \langle u_i'' u_i'' \rangle$, is shown in figure 9. Disturbance velocity and turbulent kinetic energy profiles in the upstream section of the vessel ($x < 0D$) and the far downstream region ($x > 12D$) are not included in these figures because the levels were insignificant and close to zero.

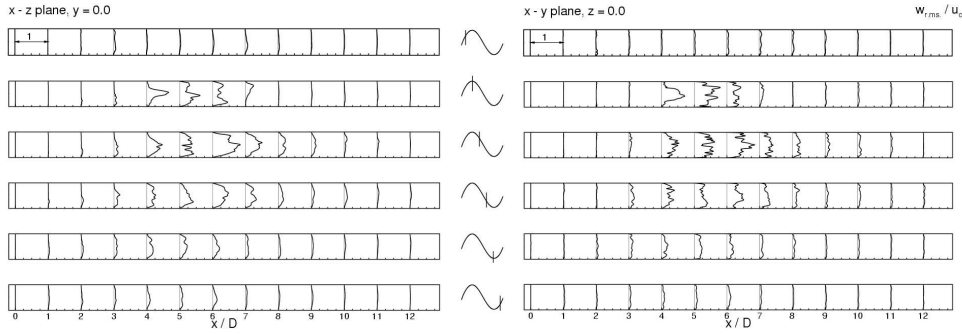
Midway through acceleration, the streamwise *r.m.s.* velocity profiles immediately downstream of the stenosis, most notably at $x = 2D$, exhibit peaks of almost $0.1u_c$ within the shear layer. Cross-stream disturbances, as indicated by $v_{r.m.s.}$ and $w_{r.m.s.}$, in the same



(a)



(b)



(c)

FIGURE 8. *R.M.S.* velocity profiles, normalized by mean inlet centerline velocity u_c , for pulsatile flow through the 75% eccentric stenosis. (a) $u_{r.m.s.}/u_c$, (b) $v_{r.m.s.}/v_c$, (c) $w_{r.m.s.}/w_c$.

region are not quite as high. Farther downstream, between $x = 3D$ and $9D$, average *r.m.s.* levels across each section lie between 5% and 15% of u_c , significantly lower than the high levels the region experienced during the transitional/turbulent activity of the previous cycle. The turbulent energy profiles, lower than 5% of u_c^2 across the entire post-

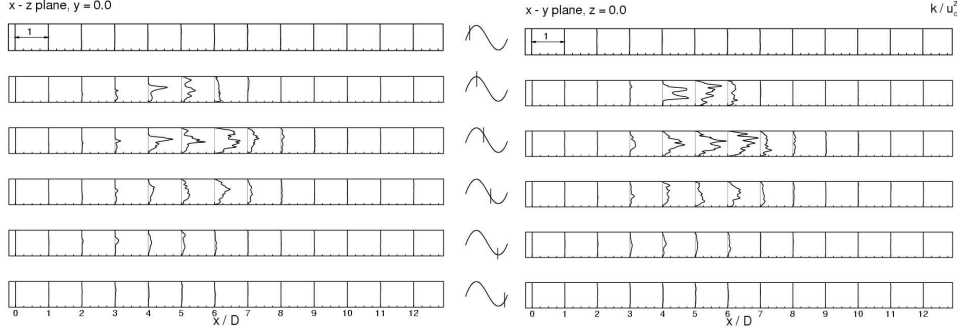


FIGURE 9. Turbulent kinetic energy (k) profiles, normalized by u_c^2 , for pulsatile flow through the 75% eccentric stenosis.

stenotic section, confirms the progress of relaminarization throughout the acceleration phase.

The end of acceleration, culminating in peak flow conditions at the inlet, witnesses a sharp amplification of the disturbance and turbulent energy levels, especially within the shear layer. Peak values of $u_{r.m.s.}$ in the $y = 0.0$ plane increase with axial distance, from about $0.25u_c$ at $x = 2D$ to more than $0.4u_c$ and $0.75u_c$ at $x = 3D$ and $4D$, respectively, while turbulent energy peaks at about $0.75u_c^2$ at the latter station. The subsequent jet breakdown after it encounters the wall spreads over the entire cross-section of the vessel, as a result of which both streamwise and cross-stream *r.m.s* velocity profiles at $x = 5D$ and $6D$ exhibit more uniformity than their immediate upstream counterparts, with mean levels now larger than $0.25u_c$. Turbulent energy profiles at the same locations show turbulent energy production peaking at $x = 5D$, the axial station at which the shear layer completely breaks up at this stage. While maximum turbulence intensities occur in the shear layer immediately downstream of the stenosis after peak flow, it is clear from comparing the phase-averaged axial velocity profiles in figure 4 with $u_{r.m.s.}$ profiles in figure 8 that the disturbance levels within the recirculation regions also start to rise during this stage. The most intense reverse flow regions experience peak $u_{r.m.s.}$ levels of $0.25u_c$ or higher. Cross-stream *r.m.s.* velocity levels, which are lower than $0.1u_c$ within the shear layer, are higher in these zones, with $v_{r.m.s.}$ as high as $0.25u_c$ and $0.5u_c$ at $x = 3D$ and $4D$, respectively. The turbulent energy profiles in the $y = 0.0$ plane also indicate a fairly significant level of turbulence production within the recirculation region at this time, with a peak of almost $0.2u_c^2$ at $x = 4D$ close to the wall.

The early deceleration stage witnesses a significant increase in turbulent energy levels between $x = 4D$ and $7D$, indicating that the transition to turbulence process accompanying jet breakdown now extends over a larger section of the post-stenotic vessel. All three components of the *r.m.s.* velocity in this turbulent region are comparable, with average levels of about $0.25u_c$ at $x = 4D$ and $0.5u_c$ at $x = 6D$ before dropping back to less than $0.25u_c$ after $x = 8D$. The maximum turbulence intensity is experienced during this phase of the pulsatile cycle in the region between $x = 5D$ and $6D$, with peak values of $u_{r.m.s.}$ more than 100% of u_c and turbulent energy peaks larger than $0.75u_c^2$. As the flow continues to decelerate, turbulence intensity starts to reduce, with average *r.m.s.* and turbulent energy levels in the turbulent section during late deceleration dropping to less than half their pre- mid-deceleration levels. Throughout the deceleration phase, mean *r.m.s.* levels within the recirculation regions between $x = 2D$ and $4D$ lie in the

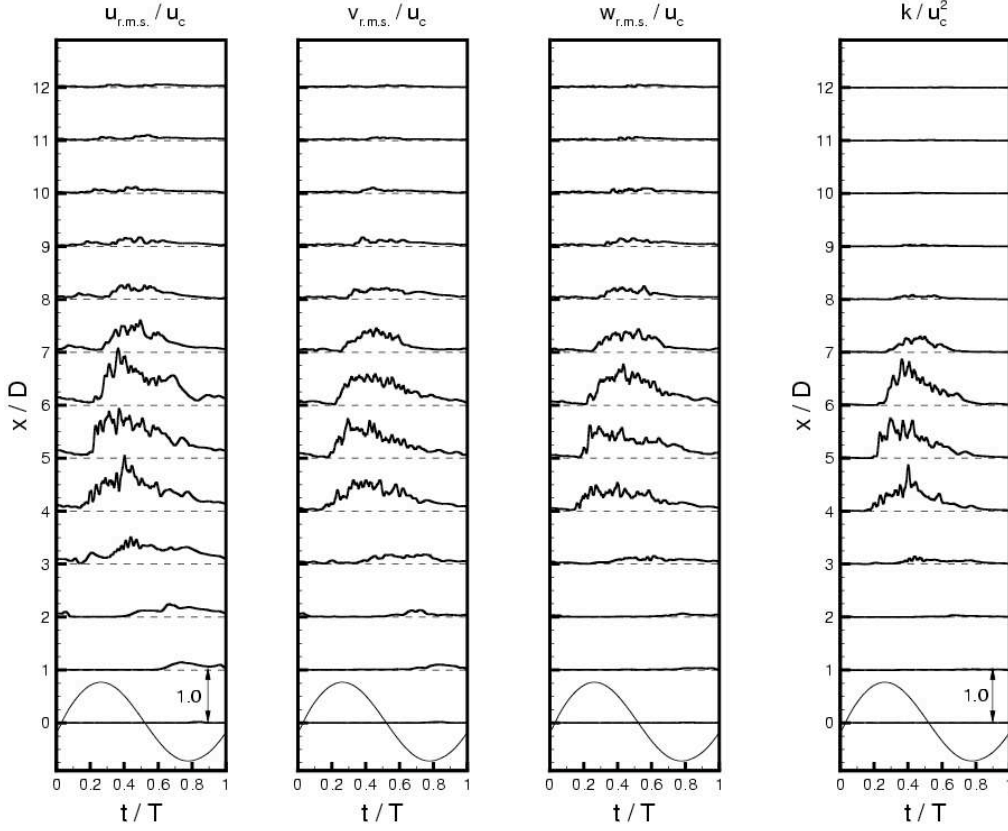


FIGURE 10. Time evolution of *r.m.s.* velocities and turbulent kinetic energy over the pulsatile cycle at axial stations along the vessel centerline for pulsatile flow through the 75% eccentric stenosis. The inlet flow waveform has been superimposed on the profile at $x/D = 0$ in order to analyze statistics during different parts of the cycle.

range $0.1 - 0.2u_c$, even though turbulent energy within these zones is lower than $0.1u_c^2$, not quite as large as that observed during peak flow conditions.

By the point of minimum inlet flow, turbulent energy levels decrease sharply to less than $0.1u_c^2$ at all stations. The streamwise *r.m.s.* velocity drops to about $0.25u_c$ between $x = 4D$ and $6D$, while average cross-stream levels at these locations also drop to less than $0.15u_c$, even as the relaminarization process starts with the reversal of the pressure gradient at this time and continues into the acceleration phase. Mean *r.m.s.* levels during early acceleration are less than 10% of u_c across the entire downstream region and remain so throughout the rest of this phase, though they indicate the presence of small disturbances even in the absence of turbulence.

Disturbance levels are clearly negligible throughout the acceleration phase in the region beyond $x = 9D$. Only during deceleration do *r.m.s.* levels between $x = 9D$ and $12D$ increase, with mean values of about $0.1u_c$ at the former station and less than $0.05u_c$ at the latter. Turbulent energy levels in this far-downstream section are close to zero throughout the cycle, indicating that the flow reverts quite rapidly to its upstream laminar state downstream of the turbulent section.

Figure 10 shows the variation of all three components of *r.m.s.* velocity and turbulent kinetic energy along the centerline of the vessel during a pulsatile cycle, providing in-

sight into the temporal evolution and periodicity of these turbulence parameters. In the immediate downstream locations, at $x = 1D$ and $2D$, streamwise disturbances rise to about $0.2u_c$ during the late deceleration stage, around minimum flow. This corresponds to the phase during which these locations experience reverse flow, as the phase-averaged centerline axial velocity results in figure 7 show. At $x = 3D$, the passage of a starting structure during the late acceleration phase is associated with $u_{r.m.s.}$ levels of about $0.2u_c$, subsequently increasing to more than $0.4u_c$ during peak flow, when breakdown starts to occur. Past mid-deceleration, when the reverse flow regions extend to the centerline at this station, cross-stream disturbances also rise to almost $0.2u_c$, comparable to the streamwise disturbances during this time, along with a corresponding increase in turbulent energy levels to about $0.1u_c^2$.

Farther downstream, for $x > 3D$, the start of the turbulent jet breakdown process at peak flow is accompanied by large streamwise *r.m.s.* velocities, which at this time are almost a factor of 2 larger than their cross-stream counterparts. Turbulence intensity along the centerline clearly reaches a maximum during the early deceleration stage, with $u_{r.m.s.}$ and energy levels attaining peaks that are as high as 100% of u_c and $0.8u_c^2$, respectively, between $x = 4D$ and $6D$. Cross-stream *r.m.s.* levels in the turbulent zone are of comparable magnitudes to the streamwise levels during the remainder of deceleration, the latter dropping to about $0.5u_c$ by mid-deceleration and $0.25u_c$ by minimum flow. Turbulent energy levels in this region also dive down during this stage and are close to zero throughout most of the acceleration phase. Centerline disturbance and energy levels are lower at $x = 7D$ and $8D$, with all statistics rising significantly only during deceleration, when transition to turbulence takes place immediately upstream of these stations. Beyond these locations, in the far downstream region, disturbance and energy levels are mostly insignificant throughout the cycle, as seen earlier while studying the profiles.

3.2.5. Energy spectra

Results presented for the steady flow case showed that energy spectra can aid in providing additional information about the nature of disturbances in the post-stenotic region. For the current pulsatile flow results, the normalized spectrum, E^* , and Strouhal number, N_s , have been defined by using the conventions followed in similar studies (Cassanova & Giddens 1978; Khalifa & Giddens 1981; Mittal, Simmons & Najjar 2003) as

$$\begin{aligned} E^* &= \frac{E(f)u_p}{2\pi d}, \\ N_s &= \frac{2\pi f d}{u_p}, \end{aligned} \tag{3.1}$$

respectively. $E(f)$ is the frequency spectra of the normalized streamwise velocity fluctuations $(\frac{u''}{u_{r.m.s.}})^2$, f is the frequency of the fluctuation, d ($= 0.5D$) is the minimum stenosis diameter and u_p is the peak cross-sectional average velocity at the stenosis throat, calculated as $\approx 4.3u_c$ using Womersley's analysis (Womersley 1955). Cassanova & Giddens (1978) postulated that d and u_p are appropriate scaling parameters for the spectra because it is the peak stenotic jet velocity that initiates the transition to turbulence in the downstream section.

The frequency spectra $E(f)$ of the velocity data in figure 7(a) was computed by using Welch's overlapping averaged modified periodogram method (Welch 1967). The data was divided into 10 segments with 50% overlap, each section windowed with a cosine taper window (Hann window) to reduce leakage, and 10 modified periodograms were computed and averaged. The data sampling rate was 2kHz, corresponding to a Nyquist frequency of 1kHz.

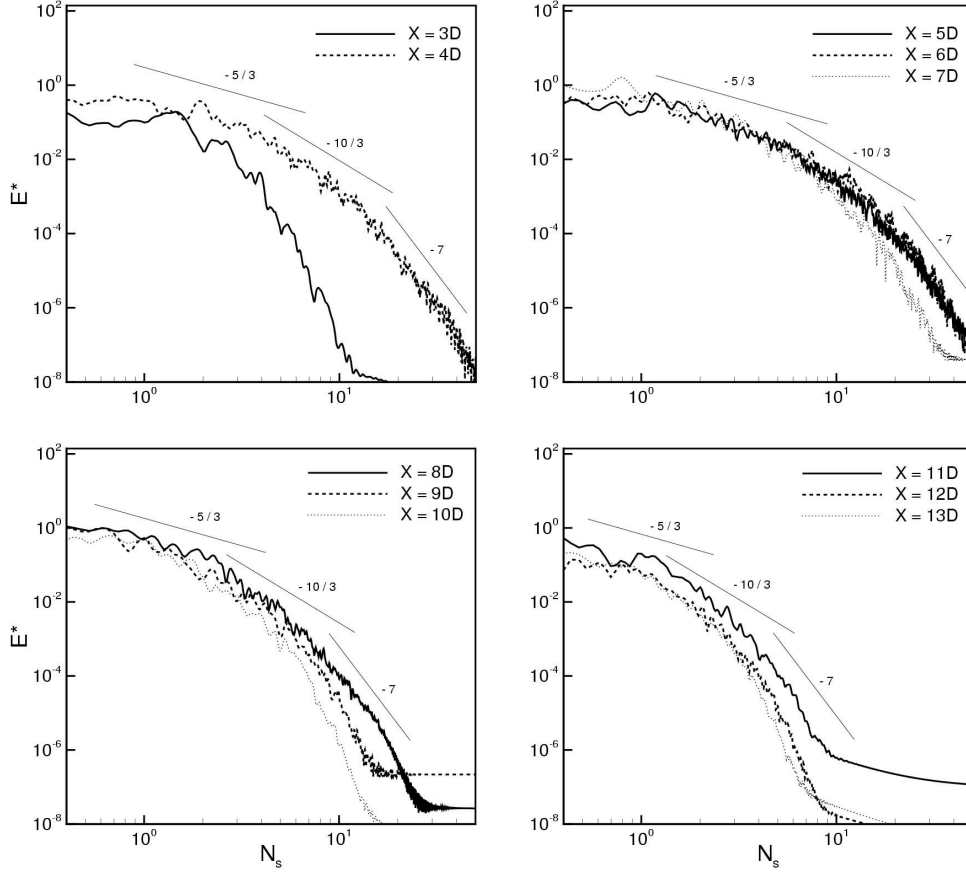


FIGURE 11. Normalized energy spectra of centerline streamwise velocity fluctuations, u'' normalized by $u_{r.m.s.}$ for pulsatile flow through the 75% eccentric stenosis.

Figure 11 shows the computed normalized centerline disturbance energy spectra at various axial stations downstream of the stenosis throat. As in the steady flow spectra, the lines corresponding to $N_s^{-5/3}$ and N_s^{-7} have been included in the figure, the former characterizing the inertial subrange, where energy cascades from the large eddies to smaller ones with minimal energy dissipation, and the latter, the viscous dissipation range (Tennekes & Lumley 1972; Hinze 1975; Wilcox 1993; Mittal *et al.* 2003). Studies of post-stenotic flow by Kim & Corcoran (1974) and Lu, Gross & Hwang (1980) have found evidence of a $N_s^{-10/3}$ range in the velocity spectra, also indicated in the figure, with the latter group observing that *in vivo* velocity spectra fell from a $-5/3$ to $-10/3$ slope at a frequency associated with arterial murmurs.

At $x = 3D$, the spectra show multiple peaks, with most of the energy concentrated within a frequency band around $N_s \approx 2.45$. The peaks are not as well-defined and concentrated within a narrow frequency range as those observed for the steady flow case in the vicinity of this same station, indicating increasingly complex vortex behavior as the structures convect downstream under pulsatile conditions. It appears that large-scale vortices coalesce together and start to breakdown in this region. The spectra at $x = 3D$ appear to roll off rapidly after $N_s \approx 2.45$ from a $-5/3$ slope to a -7 slope. Figure 12

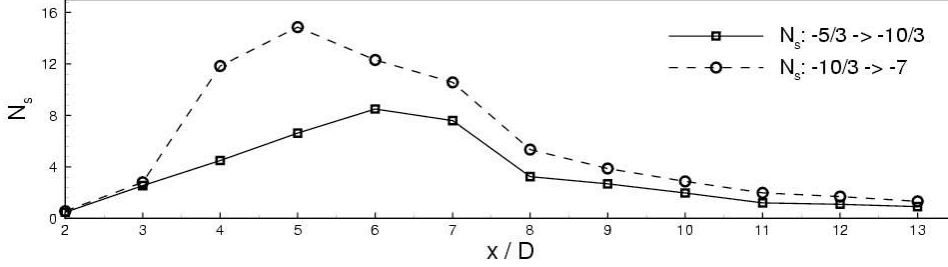


FIGURE 12. Approximate Strouhal numbers at which the energy spectrum changes its slope from $-5/3$ to $-10/3$ and from $-10/3$ to -7 at post-stenotic axial locations along the vessel centerline.

shows the approximate frequencies at which the spectra in figure 11 roll off from a $-5/3$ slope to a $-10/3$ slope, as well as from the $-10/3$ slope to a -7 slope.

The flow clearly transitions into broadband turbulence at $x = 4D$, with the spectra at this location indicating a large range of frequencies constituting the inertial subrange. The spectra roll from this range to a $-10/3$ slope rather gradually, after $N_s \approx 4.5$, eventually attaining a slope of -7 at frequencies higher than 12.0. The energy distributed at higher frequencies rises even farther after $x = 4D$, as the increasingly broadband spectra at $x = 5D$ and $6D$ highlight. The spectra at these stations roll off to a $-10/3$ slope at frequencies of 6.63 and 8.5, respectively, the large range of frequencies comprising the inertial subrange indicative of fairly well-developed turbulent flow in this region. Turbulence intensity drops rapidly farther downstream, with the spectra at $x = 7D$ and $8D$ rolling from the $-5/3$ range to a $-10/3$ slope at $N_s = 7.6$ and 3.25, respectively. With viscous effects dominating the region beyond $x = 8D$ and relaminarization taking place, the spectra in the far downstream region roll off into the viscous dissipation range at frequencies as low as $N_s \approx 1.1$. Clearly, the $-10/3$ range is largest within the turbulent part of the post-stenotic flowfield, between $x = 4D$ and $8D$, and is almost absent in the region $x > 9D$, consistent with the speculation that arterial murmurs are closely associated with turbulent flow within these arteries.

3.2.6. Turbulence structure

In this section we discuss some of the interesting features of the turbulence structures alluded to in the previous sections while discussing the spatial and temporal evolution of averaged flow characteristics and turbulent statistics. Figure 13 shows instantaneous coherent structures, as identified by isosurfaces of a negative contour of the λ_2 criterion of Jeong & Hussain (1995). Corresponding instantaneous contours of the streamwise velocity fluctuations u''/u_c are depicted in figure 14.

During the late acceleration phase, the λ_2 structures clearly show the vortex ring, which formed at the forefront of the stenotic jet earlier during acceleration, starting to deform and stretch in the streamwise direction between $x = 2D$ and $3D$. The corresponding streamwise velocity fluctuations are less than 15% of u_c across the entire downstream section of the vessel, indicating fairly quiescent flow during this time. As the flow proceeds to become increasingly unstable throughout the end of the acceleration phase, the starting vortex breaks into elongated, smooth streamwise structures that extend axially over a length of more than one vessel diameter. These vortices eventually break down into small scale structures at $x = 4D$ when the flowrate reaches its peak. By the advent of peak flow, relatively strong fluctuations are present in the shear layer between $x = 2D$ and

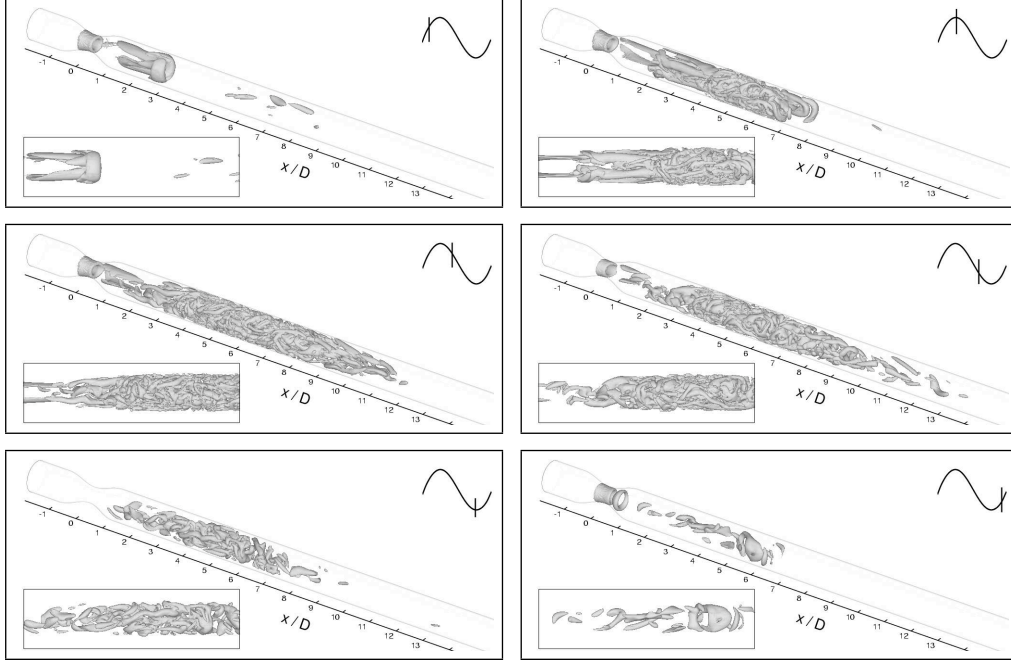


FIGURE 13. Sequence of instantaneous coherent structures (vortices) identified by using the isosurface corresponding to the negative contour -1.0 of the λ_2 criterion of Jeong & Hussain (1995), normalized by u_c/D , for pulsatile flow through the 75% eccentric stenosis. The inset in each plot shows a close-up view of the structures in the region $1D \leq x \leq 6D$.

$4D$. The unstable shear layer can be seen to roll-up before bursting into a localized turbulent spot that occupies the entire cross-section of the vessel between $x = 4D$ and $6D$. This spot-like transition of elongated streamwise structures has also been observed by Scotti & Piomelli (2001a) in their DNS studies of pulsating turbulent channel flow at low frequencies. Streamwise vortices have been shown to play an important role in the transition mechanism of stable shear and pipe flows by several investigators (Waleffe 1997; Eliahou *et al.* 1998; Shan *et al.* 1999; Han *et al.* 2000). These longitudinal rolls redistribute the streamwise momentum across the cross-stream directions, causing non-uniformity and rendering the flow unstable with respect to even small three-dimensional disturbances.

Turbulent breakdown of the structures continues into the early stages of deceleration with the turbulent spot now occupying the entire region between $x = 4D$ and $7D$. Fluctuation levels within the shear layer can be seen to be rising to a maximum during deceleration, even as the intensity of the breakdown starts to drop as the flow loses its momentum and moves past the mid-deceleration stage toward minimum flow. The turbulent spot clearly loses its strength during the late stages of deceleration and almost completely loses its coherence by the point of minimum flow. The relaminarization process starts during late deceleration itself; as a result, the subsequent acceleration phase starts with relatively low residual fluctuation levels. A new vortex ring forms immediately downstream of the stenosis throat as the flow once again starts to pick up momentum, while the remainder of the downstream section continues to undergo relaminarization.

The variation of instantaneous streamwise velocity along the vessel centerline for the eccentric model is shown in figure 15. Corresponding results for the laminar, axisymmet-

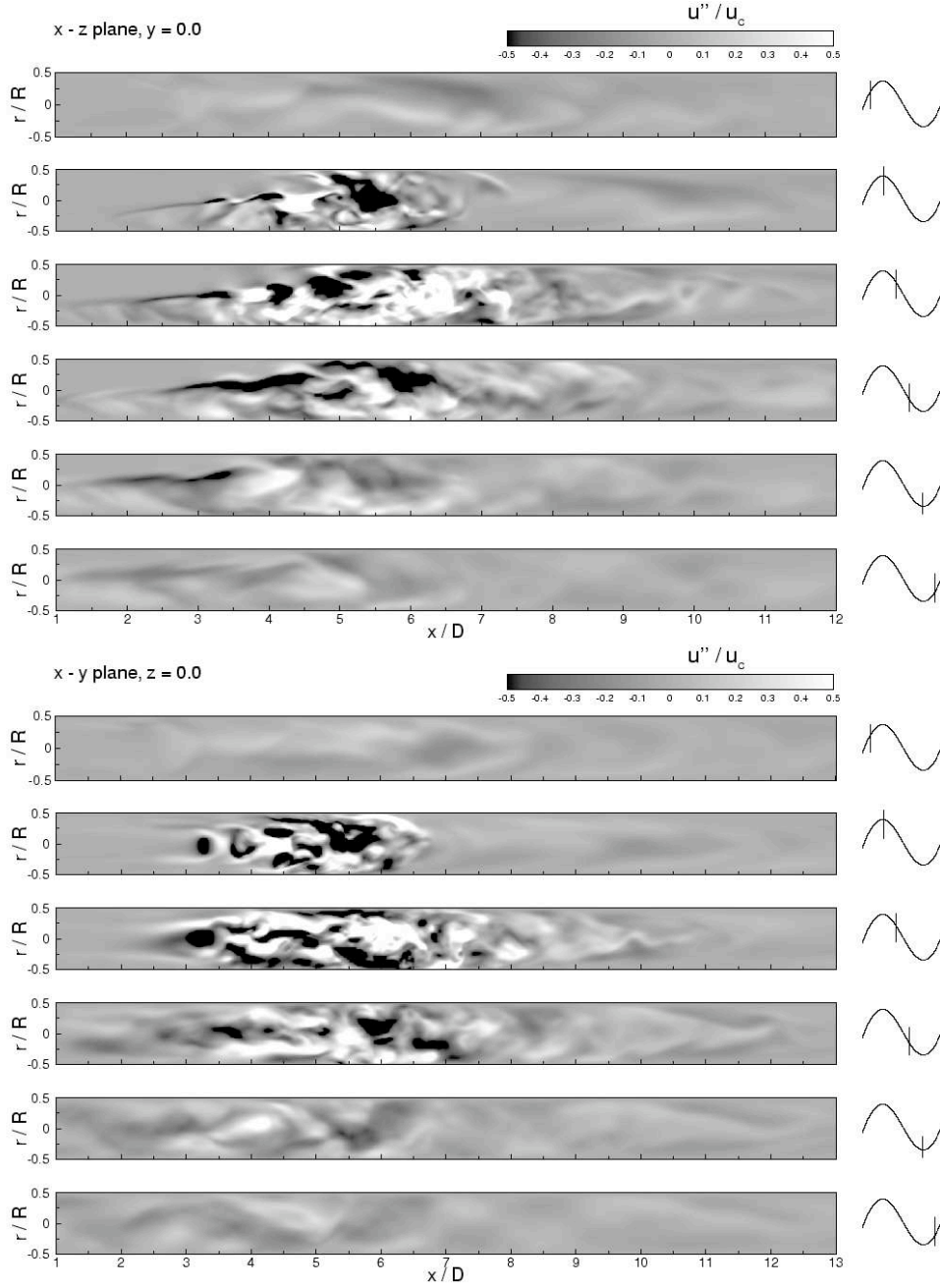


FIGURE 14. Sequence of contours of the streamwise velocity fluctuations u''/u_c , for pulsatile flow through the 75% eccentric stenosis.

ric case are also included in the figure to highlight the footprints left by the turbulent structures in the eccentric case. The flowfield is clearly laminar during the late acceleration phase, with centerline velocities for the eccentric model closely matching its laminar counterpart. The velocity reaches a peak at the throat before falling back to normal levels in the downstream section, following flow reattachment at the walls (at $x \approx 3D$).

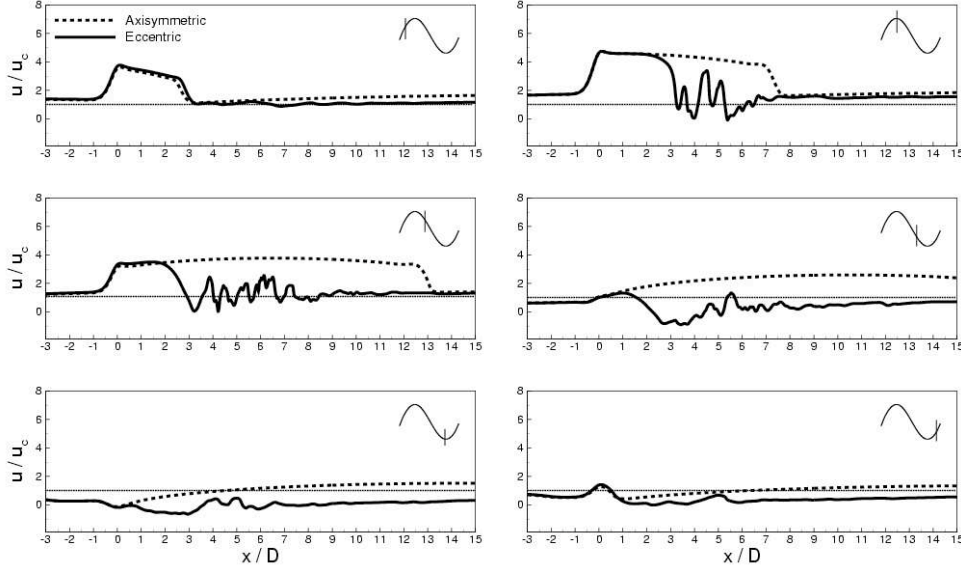


FIGURE 15. Variation of instantaneous streamwise velocity u/u_c along the centerline of the vessel, for pulsatile flow through the 75% axisymmetric and eccentric stenosis.

Residual disturbances from the previous cycle are clearly present in the region beyond $x = 7D$, where centerline velocities are lower than laminar levels, indicating that the flowfield has not quite achieved complete relaminarization.

Breakdown into turbulence after $x = 3D$ at peak flow is accompanied by a sharp drop in centerline velocity, as a result of the change in the velocity profile, from laminar upstream of the turbulent spot to a fuller turbulent flow profile inside it. The velocity signatures are in good agreement with the results of Stettler & Hussain (1986), who investigated transition in pulsatile pipe flows. The traces show the turbulent spot, or patch as they termed it, having a sharp leading front. The apparent "jetting" action of the laminar fluid into the turbulent patch produces the roll-up seen in the streamwise fluctuations of figure 14, followed by high-intensity fluctuations as turbulent breakdown occurs between $x = 4D$ and $6D$. After this breakdown, the absence of any mechanism to continue producing turbulence results in the fluctuations decaying and the flow relaminarizing, and so the trailing edge of the spot is not quite as well defined. This is in contrast to the signatures left by puffs and slugs in the transition regime of steady pipe flows (Wynagnanski & Champagne 1973; Wynagnanski, Sokolov & Friedman 1975). The former is characterized by a gradual drop in the centerline velocity as laminar flow transitions into high-frequency turbulent fluctuations within the interior of the puff. The fluctuation level drops at the trailing edge, and the velocity increases rapidly. On the other hand, a slug is associated with abrupt transition between laminar and turbulent flow at the beginning and end of the turbulent region, in relation to its duration.

In the deceleration phase, the centerline velocity deficit starts to get less distinct when compared with the traces at peak flow. The reason is that the flowrate drops during this time, and the profiles get flatter and less jet-like as a result; in other words, the difference between the centerline and mean velocity at a particular axial station starts to reduce. Hence, the jetting action is considerably weakened. Throughout the deceleration phase, the λ_2 structures in figure 13 show the presence of hairpin-like vortices near the trailing edge region of the turbulent spot. It appears that these streamwise vortex pairs

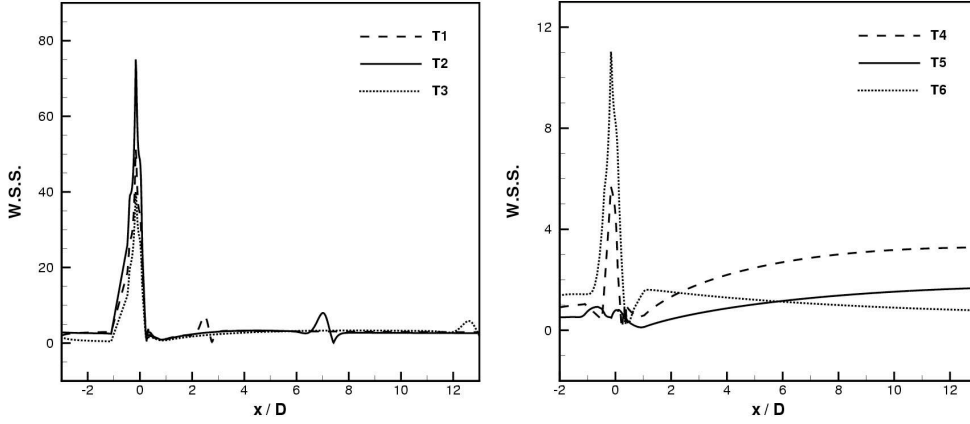


FIGURE 16. Axial variation of wall shear stress (WSS) magnitude, normalized by mean WSS upstream of the stenosis, for pulsatile flow through the 75% axisymmetric stenosis. The phases are indicated in figure 1. Note the difference in scale for the two plots.

serve to exchange fluid between the turbulent and laminar regions, contributing to the relaminarization process as the flow rate continues to drop. The intensity of turbulent fluctuations decays rapidly after the mid-deceleration phase, and at minimum flow, the fluctuations are almost completely absent. However, the flowfield has not completely relaminarized even by the early acceleration phase, with centerline velocities lower than normal.

Velocity results in figure 15 indicate that there is insufficient time for the entire post-stenotic section to regain its normal laminar self. Only in the far downstream region, $x > 8D$ under peak flow conditions and $x > 12D$ during early deceleration, do centerline velocities achieve their laminar values, indicating that the velocity profiles at these locations have indeed reverted to their natural undisturbed character. However, these disappear later in the cycle as residual disturbances from the turbulent post-stenotic region convect into the far downstream flowfield.

3.3. Wall shear stress

The flow features discussed in the previous sections directly manifest themselves in the wall shear stress (WSS) patterns across the entire vessel. Low and oscillatory WSS in particular has been implicated in arterial disease progression (Ku 1997). Figure 16 shows the axial variation of WSS at different times during the cycle, scaled by mean (cycle-averaged) upstream values to reveal the variations in shear in relation to normal, healthy arterial levels.

During the late acceleration phase and even into early deceleration, the large velocities at the throat gives rise to extremely high WSS levels within the stenosis itself. Under maximum flow conditions, they rise from their immediate upstream levels by a factor of almost thirty at the throat. This result matches well with the experimental measurements of Ahmed & Giddens (1984), who found WSS at the throat to be around thirty times upstream levels during peak inlet flow. The magnitudes drop rapidly within the diverging section of the stenosis as flow separation starts to occur. Flow reattachment results in a small jump, and subsequent dip, in the WSS profile, and this travels further downstream with the reattachment location as the cycle progresses. The magnitudes drop significantly after mid-deceleration, as the flow loses momentum. At minimum flow, throat levels are

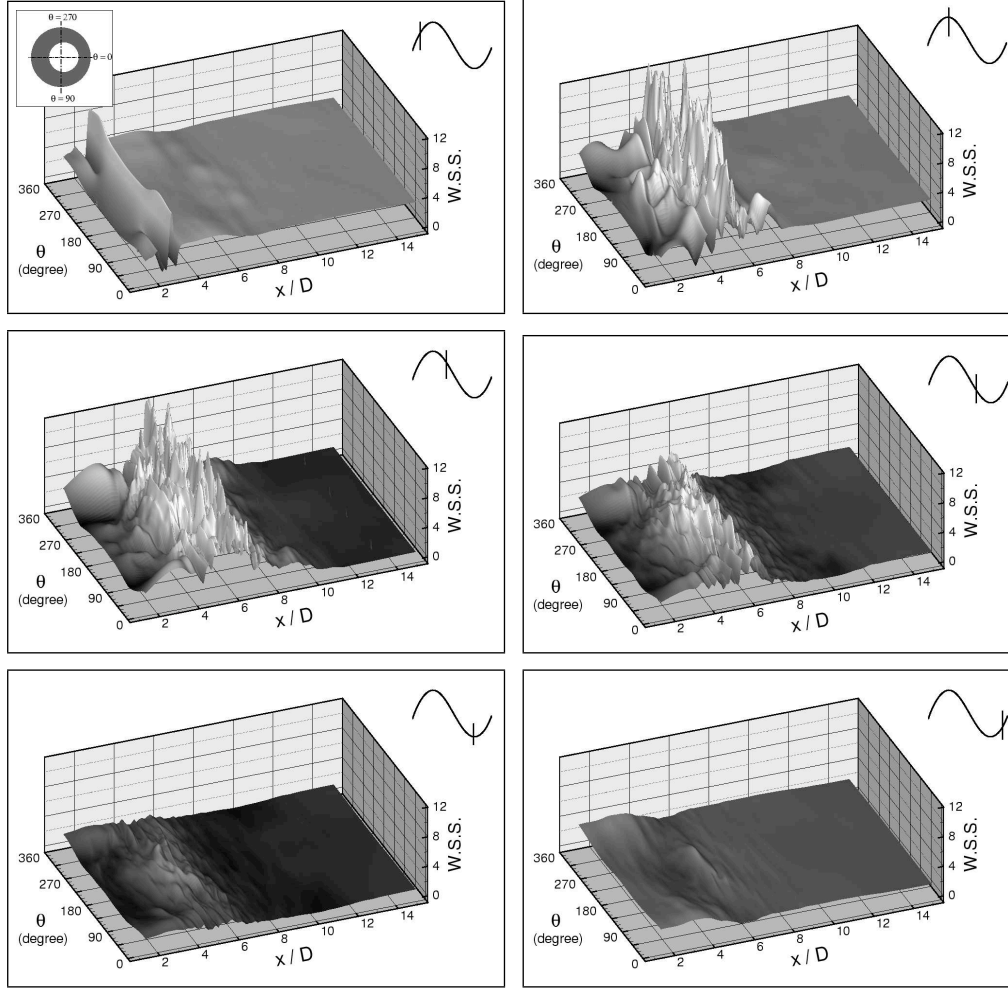


FIGURE 17. Sequence of phase-averaged WSS magnitude in the post-stenotic region ($1D \leq x \leq 15D$), highlighting the axial and circumferential distribution, for pulsatile flow through the 75% eccentric stenosis. WSS levels have been normalized by the mean WSS up-stream of the stenosis.

only about twice that of upstream values, but these start to pick up when the flow starts to accelerate once again.

In sharp contrast to the axisymmetric model, phase-averaged WSS magnitude exhibits large spatial and temporal variations in the post-stenotic region $x \geq 1D$, as figure 17 illustrates. The effect of the eccentricity is clear, with large temporal variations in both the axial and circumferential directions being readily apparent. Results in the region $-3 \leq x < 1D$ are not included in the figure because these are identical to those presented for the axisymmetric model in figure 16. The locations corresponding to the largest WSS magnitudes in the post-stenotic region follow the jet and accompanying separation zones during the acceleration phase, when the flow is relatively stable. As seen in the axisymmetric model, flow reattachment at $x \approx 2.5D$ is accompanied by an increase in stress levels. Circumferential variations are also not significant during the late acceleration phase, but the similarity between the two models ends at peak flow. Shear stress

magnitudes increase dramatically under peak inlet flow conditions, as a result of the turbulent breakdown. Large fluctuations occur between $x = 4D$ and $6D$, corresponding to the location of the turbulent spot seen in §3.2.6. WSS levels increase by a factor of seventy-five at the stenosis throat before dropping down to mean upstream levels, or even lower, in the region preceding the spot, where flow separation regions exist. They rise again in the turbulent region where magnitudes appear to be between four and twelve times higher than mean upstream levels.

The spreading of the turbulent spot during early deceleration, between $x = 4D$ and $7D$, results in the peaks and valleys coincidentally spreading over a larger region. WSS magnitudes start to reduce following mid-deceleration and at the late deceleration stage, peak levels in the turbulent section are only about four times as large as mean upstream levels. As relaminarization progresses, WSS continues to drop; at minimum flow, both axial and circumferential variations are no longer significantly large, and this is observed to be the case even in the early stages of acceleration. Throughout the cycle, the flow in the downstream region beyond the turbulent spot experience shear stress levels that are close to mean upstream values.

3.4. Comparison with previous studies

The pulsatile flow simulations were performed with flow parameters and geometry (axisymmetric) exactly the same as those used by Ahmed & Giddens (1984), and as seen in §3.1, the numerical results match very well with their laser Doppler anemometry (LDA) measurements in the region immediately downstream of the stenosis. The numerical simulations through the axisymmetric model predict laminar flow downstream of the constriction, whereas there was evidence of disturbed flow in the experiments. The experimentalists reported stable flow during the early acceleration phase, followed by the formation of periodic coherent starting structures that were shed from the stenosis. Toward the end of acceleration, discrete frequency velocity oscillations accompany this structure; and after peak flow, it was observed to break down into turbulence at $x \approx 6D$. This scenario closely resembles the one predicted by the numerics for the eccentric model under similar flow conditions, presented in §3.2.

Numerical results for the axisymmetric model predict flow reattachment between $x = 7D$ and $8D$ under peak flow conditions, whereas in the experiments, reattachment was found to occur between $x = 5D$ and $6D$. However, simulations with the eccentric model showed reattachment occurring in exactly the same region as the experiments during peak flow, illustrated by phase-averaged velocity profiles in figure 4, indicating that transition to turbulence during this stage of the cycle promotes reattachment closer to the stenosis than in the corresponding laminar situation. This explains the small disagreement between the computed and experimental profiles in figure 3 at $x = 6D$. As in the experiments, the numerics for the axisymmetric and eccentric model predict small flow separation upstream of the constriction during the late deceleration phase, close to minimum flow. In contrast to its steady flow counterpart, pulsatile flow through both models indicate the absence of a permanent recirculation zone, with forward flow occurring across the entire vessel during the early acceleration phase, an observation also made by the experimentalists.

Earlier investigations by Cassanova & Giddens (1978) and Khalifa & Giddens (1981) characterized post-stenotic flow disturbances for pulsatile flow through an axisymmetric 75% smooth stenosis model similar to the one used here. Their studies had minimum and peak Reynolds number close to 500 and 2240, respectively, and Womersley parameters of $\alpha = 15$ in the former study and $\alpha = 8.4$ in the latter. These flow parameters are in contrast to corresponding Reynolds numbers of 200 and 600 and $\alpha = 7.5$ employed in this

study, but the post-stenotic flow behavior is strikingly similar. Khalifa & Giddens (1981) identified three distinct types of flow disturbances in the downstream flowfield: a coherent startup structure that formed at the beginning of each new cycle, shear layer oscillation due to flow separation, and turbulence. They reported that "turbulence appeared to rapidly interact with the starting structure, having evolved from a laminar oscillation which exists in the very near post-stenotic field". Centerline velocity waveforms from both studies qualitatively match our results for the eccentric case in figure 7, with evidence of the startup structure seen at immediate downstream stations, followed by high-frequency fluctuations after $x \approx 3D$ at peak flow, and during early deceleration. The disturbances start to dissipate toward the end of deceleration at all locations.

Another relevant comparison can be made with the flow visualization results of Ojha *et al.* (1989) who also studied pulsatile flow through a 75% axisymmetric sharp-edged constriction with $\alpha = 7.5$ and mean and modulation Reynolds numbers of 575 and 260, respectively. We note that these Reynolds numbers were based on average cross-sectional velocity at the inlet while the corresponding values used in this study, 600 and 400, respectively, are based on inlet centerline velocity. Similar to our findings for the eccentric model, this group observed that flow in the jet region, extending to $x \approx 3D$, appeared to be quite stable, with centerline velocities at these locations exhibiting a nearly sinusoidal variation. Kelvin-Helmoltz vortex roll-ups observed in this stable jet zone closely resemble those seen in the vorticity magnitude and streamwise velocity fluctuation contours illustrated in figure 5 and figure 14, respectively, during the late acceleration stage and at peak flow.

The experimental flow was in a transitional state throughout the cycle between $x = 3D$ and $4.5D$. Ojha *et al.* (1989) found that the reattachment location moved further downstream to $x \approx 4.5D$ close to minimum flow, where transition to turbulence was triggered by streamwise vortices generated earlier in the shear layer. Maximum turbulence occurred for about three vessel diameters after $x = 4.5D$, with the flow relaminarizing beyond $x = 7.5D$. These results agree closely with the current study, in which streamwise vortices were found to play an important role in the transition process at $x \approx 4D$. The turbulent statistics in § 3.2.4 showed that turbulence intensity is indeed maximum between $x = 5D$ and $6D$ after peak flow, in the vicinity of the reattachment point, followed by relaminarization in the region beyond $x = 8D$. Complete flow relaminarization within the turbulent zone is not achieved because of insufficient time, and the *r.m.s.* profiles in figure 8 confirm the presence of small disturbances in this region during the acceleration phase, subsequently contributing to the transition process at peak flow. Ojha *et al.* (1989) reported the presence of a permanent recirculation zone in the immediate downstream region as well as earlier transition to turbulence, in other words closer to the constriction than in the current simulations. These differences may be attributed to the higher mean Reynolds number employed by Ojha *et al.* (1989) in their experiments and their stenosis geometry.

Non-dimensional energy spectrum correlations by Cassanova & Giddens (1978) and Khalifa & Giddens (1981) showed broadband turbulent spectra after $x = 3D$, with a $-5/3$ slope over a broad range of frequencies, similar to those presented in § 3.2.5. The latter group observed spectral peaks in the immediate vicinity of the constriction at a Strouhal number ($St = fd/u_p$) of 0.35, corresponding to passage of the startup structure through these locations. Mittal *et al.* (2003) conducted large eddy simulations (LES) of pulsatile flow (with peak Reynolds number of 2000 and $\alpha = 8.6$) through a planar channel with a one-sided semicircular constriction and observed vortex shedding at a frequency of 0.45. The spectrum at $x = 3D$ in 11 shows a broad peak at $St \approx 0.39$, agreeing well with these studies. The presence of a $-10/3$ region in the spectra of stations in

the turbulent zone also matches the findings by Lu *et al.* (1980), who computed spectra from *in vivo* velocity measurements in six calves in the vicinity of a surgically induced pulmonic stenosis.

In a quite recent stability analysis study of pulsatile flow through an axisymmetric stenosis model similar to that considered here, albeit at mean Reynolds number of 400 (based on average cross-sectional inlet velocity) and Womersley parameter of 15.9, Sherwin & Blackburn (2004) identified the nature of the instability in such flows as a tilting mechanism of the vortex ring generated during each pulsatile cycle at the forefront of the stenotic jet. This instability resulted in a rapid distortion of the vortex ring within a few diameters downstream of the stenosis and localized turbulent breakdown at $x \approx 6D$, followed by relaminarization in the far downstream region. Our observations that were made downstream of the eccentric stenosis model are consistent with this mechanism. While Sherwin & Blackburn (2004) introduced the instability by superimposing an unstable eigen mode on a stable base flow, the source of instability in this study was the eccentricity introduced at the stenosis throat, which tilts and distorts the vortex ring as it is ejected from the constriction. Similarly, geometric asymmetries or upstream noise may be responsible for transition to turbulence in the experiments by Ahmed & Giddens (1984). The simulations by Sherwin & Blackburn (2004) also demonstrated that the instability was subcritical, implying that turbulent flow can occur at lower Reynolds numbers than the critical value of 500. This phenomenon would explain the persistence of turbulence in the current simulations, in which the mean (cycle-averaged) Reynolds number was only 300 (based on average cross-sectional inlet velocity).

Ahmed & Giddens (1984) found that wall shear stress levels in the vicinity of flow reattachment and turbulent regions were close to upstream levels, whereas Ojha *et al.* (1989) reported that instantaneous values in the turbulent section reached a value three times higher than upstream levels. Our results in §3.3 indicate that wall shear stress magnitudes in the turbulent section are anywhere between four and twelve times those of upstream levels. This is closer to the photochromic measurements of Ojha *et al.* (1989), who suggested that the LDA technique employed by Ahmed & Giddens (1984) may not be most suitable for measuring shear stress along the walls, because of difficulties associated with positioning the sample volume within the viscous sublayer.

4. Conclusions

Direct numerical simulations (DNS) have been used to study pulsatile flow through smoothly contoured 75% stenosed vessels. Similar to the steady flow studies discussed in Part 1 of this study (Varghese, Frankel & Fischer 2005), DNS predicted a completely laminar post-stenotic flowfield in the case of the axisymmetric stenosis model. Comparing axial velocity profiles with previous experimental measurements, we found good agreement in the region immediately downstream of the stenosis, but this veered off in the vicinity of flow reattachment. Flow reattachment was found to occur further away from the stenosis in the case of the numerics, when compared to reattachment locations observed in the experiments, in which intermittent disturbed flow regions and turbulent breakdown were observed to occur around six diameters downstream from the throat ($x \approx 6D$).

The introduction of a stenosis eccentricity, that was 5% of the main vessel diameter at the throat, resulted in jet breakdown and periodic, localized transition to turbulence. Analysis of the flowfield at different times during the time periodic cycle indicated that the early and mid-acceleration phases were relatively stable, with no turbulent activity in the post-stenotic region. However, during the late stages of acceleration, close to peak

flow, the shear layer started to become unstable. The starting vortex formed during early acceleration, at the jet forefront as the fluid accelerated through the stenosis, started to break up into elongated streamwise structures, though the flow remained laminar at this point. Under peak inlet flow conditions, the streamwise vortices broke down, forming a turbulent spot between $x = 4D$ and $6D$, which continued to spread to about $x = 7D$ during early deceleration. Beyond $x = 7D$, the turbulent fluctuations and energy levels rapidly decayed and flow almost completely reverted to its laminar character after $x = 11D$. Broadband velocity fluctuation spectra at axial stations within the spot confirmed turbulent flow, following the $-5/3$ energy cascade. By the advent of peak flow, large recirculation regions, continuously evolving in time and space, formed downstream of the stenosis and these were present through most of the deceleration phase. Turbulent breakdown during this time also resulted in early flow reattachment (relative to the axisymmetric case), occurring between $x \approx 6D$ and $7D$, similar to the experiments.

Turbulence intensity within the spot reduced as inlet flow lost its momentum, past the mid-deceleration stage and through to minimum flow, and the post-stenotic flow-field began to relaminarize. This process continued into the early acceleration phase, during which time forward flow existed at all locations within the vessel. The absence of a permanent recirculation zone, in both the axisymmetric and eccentric models, is in agreement with experimental findings and in contrast to steady inlet flow observations. Residual fluctuations from the turbulent activity that occurred earlier in the cycle were at their lowest past the mid-acceleration point, though results indicate that there appears to be insufficient time for the the post-stenotic section between the throat and $x \approx 9D$ to regain its normal laminar state, similar to the flowfield upstream of the stenosis.

Variation of wall shear stress magnitudes at the stenosis throat were close to experimental measurements. However, in contrast to the axisymmetric case, WSS magnitudes exhibited large spatial and temporal variations in the region $x > 1D$ for the eccentric model. Peak levels in the post-stenotic region occurred in the vicinity of flow reattachment, continuously moving further away from the stenosis as acceleration progressed. Circumferential variations were not significant during this phase of the cycle. Turbulent breakdown of the stenotic jet at peak flow and during early deceleration resulted in a sharp increase in WSS levels, with large axial and circumferential fluctuations occurring in the region between $x \approx 4D$ and $7D$, corresponding to the location of the turbulent spot. WSS magnitudes were anywhere between four and twelve times higher than mean upstream levels in the turbulent region but these levels dropped rapidly as relaminarization took over during the remainder of the cycle.

Our study shows that a post-stenotic flowfield rich in flow features such as recirculation, strong shear layers and periodic turbulent breakdown, manifests itself on wall shear stress by way of large spatial and temporal gradients, implicated in the progression of atherosclerotic disease (Ku 1997; Wootton & Ku 1999). The detailed representation and analysis of the flowfield downstream of a clinically significant, albeit idealized, stenosis under physiologically realistic flow conditions (as defined by the Reynolds and Womersley numbers), complements earlier stenotic flow studies and serves as basis for understanding the complex flowfields that may arise in realistic arterial geometries. Comparison with earlier work suggests that the mechanics of turbulent breakdown, in terms of turbulent statistics, spectral correlations and the evolution of coherent structures downstream of the stenosis, is independent of the nature in which it was brought about; be it a geometric perturbation such as a stenosis eccentricity or a perturbed inlet flow upstream of the stenosis, both of which are extremely relevant from the physiological point of view because real-life stenosed arteries are unlikely to exhibit any axisymmetry and nor is the upstream flow likely to resemble laminar, undisturbed, fully developed pipe flow. The DNS results

presented in this study, along with those in Part 1, also provide a valuable database for validating turbulence models that can subsequently be employed to predict biofluid flows, and particularly stenotic flows such as those considered here, to an acceptable level of accuracy.

REFERENCES

- AHMED, S. A. & GIDDENS, D. P. 1983a Velocity measurements in steady flow through axisymmetric stenoses at moderate Reynolds number. *J. Biomech.* **16**, 505–516.
- AHMED, S. A. & GIDDENS, D. P. 1984 Pulsatile poststenotic flow studies with laser Doppler anemometry. *J. Biomech.* **17**, 695–705.
- CASSANOVA, R. A. & GIDDENS, D. P. 1978 Disorder distal to modeled stenoses in steady and pulsatile flow. *J. Biomech.* **11**, 441–453.
- ELIAHOU, S., TUMIN, A. & WYGNANSKI, I. 1998 Laminar-turbulent transition in Poiseuille pipe flow subjected to periodic perturbation emanating from the wall. *J. Fluid Mech.* **361**, 333–349.
- FISCHER, P. F., KRUSE, G. & LOTH, F. 2002 Spectral element methods for transitional flows in complex geometries. *J. Scientific Computing* **17**, 81–98.
- HAN, G., TUMIN, A. & WYGNANSKI, I. 2000 Laminar-turbulent transition in Poiseuille pipe flow subjected to periodic perturbation emanating from the wall. Part 2. Late stage of transition. *J. Fluid Mech.* **419**, 1–27.
- HINZE, J. O. 1975 *Turbulence*. McGraw-Hill.
- JEONG, J. & HUSSAIN, F. 1995 On the identification of a vortex. *J. Fluid Mech.* **285**, 69–94.
- KHALIFA, A. M. A. & GIDDENS, D. P. 1981 Characterization and evolution of post-stenotic flow disturbances. *J. Biomech.* **14**, 279–296.
- KIM, B. M. & CORCORAN, W. H. 1974 Experimental measurements of turbulence spectra distal to stenoses. *J. Biomech.* **7**, 335–342.
- KU, D. N. 1997 Blood flow in arteries. *Ann. Rev. Fluid Mech.* **29**, 399–434.
- LIEBER, B. B. & GIDDENS, D. P. 1988 Apparent stresses in disturbed pulsatile flows. *J. Biomech.* **21**, 287–298.
- LU, P. C., GROSS, D. R. & HWANG, N. H. C. 1980 Intravascular pressure and velocity fluctuations in pulmonic arterial stenosis. *J. Biomech.* **13**, 291–300.
- MITTAL, R., SIMMONS, S. P. & NAJJAR, F. 2003 Numerical study of pulsatile flow in a constricted channel. *J. Fluid Mech.* **485**, 337–378.
- OJHA, M., COBBOLD, C., JOHNSTON, K. & HUMMEL, R. 1989 Pulsatile flow through constricted tubes: An experimental investigation using photochromic tracer methods. *J. Fluid Mech.* **13**, 173–197.
- SCOTTI, A. & PIOMELLI, U. 2001a Numerical simulation of pulsating turbulent channel flow. *Phys. Fluids* **13**, 1367–1384.
- SHAN, H., MA, B., ZHANG, Z. & NIEUWSTADT, F. T. M. 1999 Direct numerical simulation of a puff and a slug in transitional cylindrical pipe flow. *J. Fluid Mech.* **387**, 39–60.
- SHERWIN, S. J. & BLACKBURN, H. M. 2004 Three-dimensional instabilities of steady and pulsatile axisymmetric stenotic flows. *Submitted to J. Fluid Mech.*
- STETTTLER, J. C. & HUSSAIN, A. K. M. F. 1986 On transition of the pulsatile pipe flow. *J. Fluid Mech.* **170**, 169–197.
- TENNEKES, H. & LUMLEY, J. L. 1972 *A First Course in Turbulence*. MIT Press.
- VARGHESE, S. S., FRANKEL, S. H. & FISCHER, P. F. 2005 Direct numerical simulation of stenotic flows, Part 1: Steady flow. *Preprint*.
- WALEFFE, F. 1997 On self-sustaining process in shear flows. *Phys. Fluids* **9**, 883–900.
- WELCH, P. D. 1967 The use of fast Fourier transform for the estimation of power spectra: A method based on time averaging over short modified periodograms. *IEEE Trans. Audio Electroacoustics*, vol. AU-15, pp. 70–73.
- WILCOX, D. 1993 *Turbulence modeling for CFD*. La Cañada, California, CA: DCW Industries.
- WOMERSLEY, J. R. 1955 Method for the calculation of velocity, rate of flow and viscous drag in arteries when the pressure gradient is known. *J. Physiology* **127**, 553–563.

- WOOTTON, D. M. & KU, D. N. 1999 Fluid mechanics of vascular systems, diseases, and thrombosis. *Annu. Rev. Biomed. Eng.* **1**, 299–329.
- WYGNANSKI, I. J. & CHAMPAGNE, F. H. 1973 On transition in a pipe. Part 1. The origin of puffs and slugs and the flow in a turbulent slug. *J. Fluid Mech.* **59**, 281–335.
- WYGNANSKI, I. J., SOKOLOV, M. & FRIEDMAN, D. 1975 On transition in a pipe. Part 2. The equilibrium puff. *J. Fluid Mech.* **69**, 283–304.